Catalysis on microstructured surfaces: Pattern formation during CO oxidation in complex Pt domains

M. D. Graham,* M. Bär, and I. G. Kevrekidis†
Department of Chemical Engineering, Princeton University, Princeton, New Jersey 08544-5263

K. Asakura,‡ J. Lauterbach, H.-H. Rotermund, and G. Ertl
Fritz-Haber-Institut der Max-Planck-Gesellschaft, Faradayweg 4-6, 14195 Berlin, Germany
(Received 26 August 1994)

The exploration of pattern formation by reaction-diffusion systems in complex bounded domains has begun only recently. While theoretical and numerical information points to a strong interaction between patterns and boundaries, experiments are rare and for heterogeneous catalytic reactions practically nonexistent. By constructing (using microlithography) catalytic surfaces of arbitrary shape and size, we are able to study this interaction for the catalytic oxidation of CO on Pt(110). Experiments along these lines shed light on issues such as anisotropic diffusion and the behavior of individual defects. In addition, certain geometries give rise to patterns that have not been observed on the untreated catalyst and bring to light surface mechanisms that have no analog in homogeneous reaction-diffusion systems. Simple domains of controlled size constitute paradigms that make the comparisons between theory and experiment more fruitful, as we demonstrate through modeling and simulation of such examples. This approach opens the way for systematically probing certain aspects of pattern formation unique to heterogeneous catalysis.

PACS number(s): 05.40.+j, 82.20.Mj, 82.65.Jv

I. INTRODUCTION

Nonlinear reaction-diffusion systems are capable of spontaneously forming a wealth of spatiotemporal patterns [1,2], ranging from Turing patterns [3–5], spiral waves and target patterns [6–9] to "chemical turbulence" [10,11] and labyrinthine patterns [12–15]. The size and the shape of the domain are important factors in these systems, as they are in essentially every nonlinear pattern forming system (e.g., in Rayleigh-Bénard convection and other hydrodynamic instabilities; see [2] and references therein). The ratio of the geometric domain size to some intrinsic system length scale plays a central role in the theoretical study of instability and pattern formation. It becomes a crucial factor away from asymptotic (very large or very small) limiting values, when the geometric domain size is comparable to the spontaneous pattern wavelength that would be formed in an unbounded medium.

In this paper a study of the interaction of domain (boundary) geometry with spontaneous pattern formation in heterogeneous catalysis is presented. Microlithography was used to create a variety of reacting domains of controlled size and shape on polycrystalline Pt and on Pt(110) single crystals. In these microdesigned domains, we studied pattern formation during the isothermal, catalytic oxidation of carbon monoxide at low pressures (less than 10^{-3} mbar).

In the absence of boundaries, solitary pulses, spiral waves, and target patterns [16–21] with typical size on the order of several micrometers are observed in this strictly two-dimensional (2D) system, in accordance with established 2D reaction-diffusion phenomenology (see, e.g., [1]). In addition, standing waves of complex structure, "turbulence," and other patterns are found on the untreated crystal [9,17], which are presumably due to surface physical and chemical mechanisms beyond traditional reaction-diffusion models. The study of mesoscopic spatiotemporal variations in this size range for metal catalyst surfaces, such as Pt, has been made possible through the application of spatially resolved surface analysis techniques such as photoemission electron microscopy in the late 1980s [22]. In a typical crystal sample of 1 cm^2 area, many patterns and many surface defects (e.g., scratches and dislocations) interact dynamically at any moment.

From a modeler's point of view, it is desirable to systematically study the behavior as its complexity gradually increases. This can be done by controlling the ratio of natural and imposed length scales, as is routinely done in fluid mechanics (e.g., experiments in thermal convection at various container sizes). The addition of boundaries enables us to study the influence of various geometries on different aspects of the pattern formation: (a) elucidation of individual components of the dynamics, e.g., by isolating and studying the behavior of a single traveling pulse

*Permanent address: Department of Chemical Engineering, University of Wisconsin, Madison, WI 53706.
†Author to whom correspondence should be addressed.
‡Permanent address: Research Center for Spectrochemistry, Faculty of Sciences, University of Tokyo, Hongo, Bunkyo-ku, Tokyo 113, Japan.

or a single surface defect; (b) controlled study of the *interaction* between patterns and boundary conditions, such as the bouncing of fronts off walls, or the formation of periodic waves within a regular lattice of obstructions; and (c) discovery of phenomena that have not been observed on the unbounded surface.

Despite the importance of the interaction of boundaries with reaction-diffusion patterns, there have been few experimental attempts in this direction. Reaction-diffusion patterns in simple domains have been investigated in the homogeneous Belousov-Zhabotinsky (BZ) reaction [in a ring and a 1D (Couette) reactor] [23,24] and in nonisothermal catalytic reactions (e.g., catalytic oxidation of H_2 on Ni rings, ribbons and disks [25–27], and NH_3 oxidation on Pt wires [28]). Early experiments on interactions between reaction-diffusion patterns and inactive domains in the BZ reaction were described by Linde and co-workers [29,30]. A recent paper by Zhabotinsky, Eager, and Epstein [31] explores reflection and refraction of fronts at an interface between two reacting media. The interaction of traveling pulses with sudden expansions of their bounding domains was recently reported by Toth, Gaspar, and Showalter [32]. Zuburtikudis and Saltsburg [33] used nanofabrication techniques to study finite (~ 10 nm) size effects in the rate of ethane hydrogenolysis; mesoscopic-scale diffusion does not play a role at this essentially "small cluster regime" and the fundamental reason for these size effects lies more in changes in basic chemistry.

On the other hand, a number of computational papers has appeared [34–38] for pattern formation in complicated domains, which model phenomena that range from the interaction of a spiral wave with domain walls to the "diffraction" of pulses passing through orifices. The importance of boundaries on the formation of spiral waves is underlined by recent experimental results [39], which provide evidence that wave trains encountering domain corners may lead to spiral wave formation. In a recent publication we introduced an approach to studying the effects of boundaries on pattern formation for heterogeneous catalytic reactions [40]. Here we present a more extensive report, along with initial modeling and simulation results for pattern formation during CO oxidation in complex-geometry catalytic Pt domains.

This paper is organized as follows. We start with a brief description of the fabrication of the catalyst and the experimental procedure. Experimental observations are then presented, starting with comparatively large domains, where the interaction of pattern formation and geometry is not very pronounced, and proceeding towards domains in which this interaction becomes stronger. We also present a number of cases where phenomena not yet described by current reaction-diffusion modeling are observed. The experimental results are followed by a numerical simulation of two nontrivial geometries: a quasi-one-dimensional ring, around which a single pulse travels, and a regular grid of inert obstructions interacting with concentration waves. The results are summarized and some open questions posed by this work are presented along with a brief description of current efforts towards answering them.

II. EXPERIMENT

The experiments were performed on a polycrystalline platinum foil and on a Pt(110) single crystal, which have also been used in previous investigations [20,21]. An 80–100-nm-thick titanium layer (see Fig. 1) was deposited on the Pt surface and microscopic regions of bare Pt were created by hydrogen fluoride solution etching through the titanium using a negative photo resist process. The sample was transferred into an UHV chamber and the surface was cleaned by standard procedures. Throughout the reaction its temperature was kept constant to within 0.1 K. An inert thin layer of titanium oxide formed on the surface of the Ti mask.

The evolution of spatial patterns was followed with a photoemission electron microscopic (PEEM) [22]. This instrument combines high temporal (25 ms, limited by

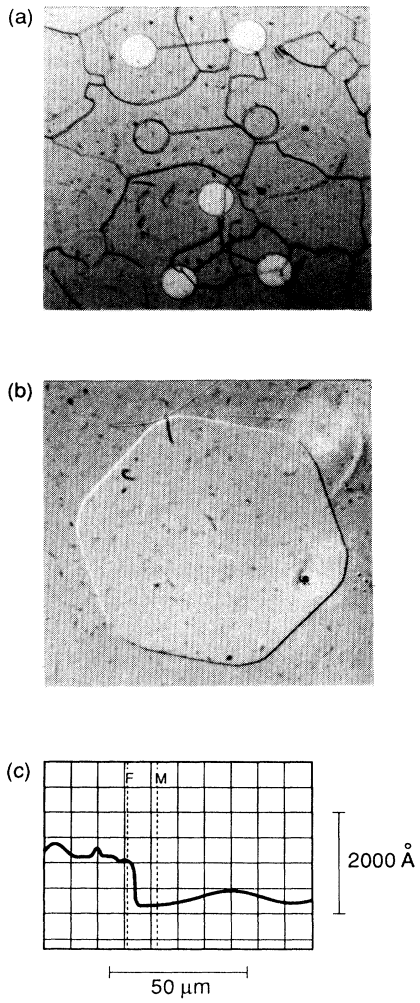

FIG. 1. Photographs of the treated Pt surfaces: (a) dumbell- and three-lobed dumbell-shaped domains on the polycrystalline sample (the picture size is 800×800 μm^2 and the dark lines are the grains boundaries) and (b) hexagonal domain on the Pt(110) single crystal surface (the picture size is 225×225 μm^2). (c) shows a depth profile across a domain boundary. The titanium layer is to the left, the pure Pt surface to the right.

the video frequency) and spatial (0.2 μm) resolution with a field of view of up to 800 μm. The contrast in the PEEM images stems from local differences in the work function caused by the different adsorbates and adsorbate coverages. In the PEEM pictures, oxygen-covered regions of the catalyst appear dark, while CO-rich areas appear lighter gray. The data were recorded on S-VHS videotapes and digitized for further image processing.

III. RESULTS AND DISCUSSION

A quick summary of the types of spatiotemporal patterns observed for CO oxidation on the Pt(110) surface is presented in Fig. 2, in the form of a qualitative two-parameter diagram [20,41], which shows the existence of various patterns at constant $p_{O_2}=4.0\times10^{-4}$ mbar as a function of the temperature and the CO partial pressure. A generic scenario of pattern formation was found at this constant p_{O_2} for temperatures between 400 and 500 K: upon an increase of the CO pressure, first elliptic CO fronts appear on the otherwise oxygen-covered surface. This leads eventually to CO-covered surface regions, on which, in turn, oxygen fronts are frequently observed. Such behavior is termed *front multiplicity* or *dynamic bistability* [42–44]. In the regime where fronts are observed, oxygen fronts are always *faster* than CO fronts and tend to catch up with and annihilate the latter. A further increase of CO pressure leads to a less pronounced difference in the velocities of CO and O fronts and to the formation of incipient stable pulses (which can be regarded as bound states, composed of the two front solutions) and eventually to spiral waves. This transition between fronts and spiral waves is well understood both in the experimental and the reaction-diffusion modeling context [45]. The spiral wave regime terminates at some upper value of the CO pressure and the surface becomes predominantly CO covered.

Using standard reaction-diffusion terminology [1], we can state that in the CO oxidation on Pt(110) spiral waves exist both under *bistable* and *excitable* conditions. Based on the absence of fronts (indicative of bistability) at the CO-covered upper left-hand part of Fig. 2, we argue that

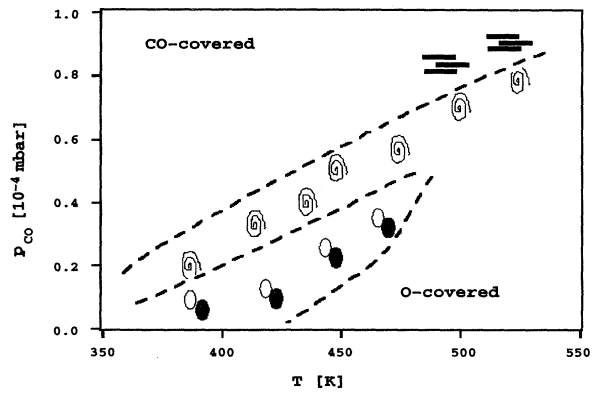

FIG. 2. Two-parameter diagram for constant $p_{O_2}=4.0\times10^{-4}$ mbar. The pictograms stand for spirals, coexisting CO and O fronts, and solitary flat waves (adapted from [20]).

the boundary between excitability and bistability lies somewhere in the spiral region (for additional evidence consult [20,41]). Quasi-one-dimensional patterns (flat solitary waves, marked by parallel bars just above the spiral waves in the figure) are formed at sufficiently high temperatures ($T>480$ K, upper right-hand corner of the diagram); this would correspond to the "low-excitability" limit. These waves propagate only along the [001] crystal axis, thus emphasizing the anisotropy of the Pt(110) surface. The diagram in Fig. 2 does not capture the region above 540 K, where phenomena such as standing waves and turbulencelike behavior are seen [9,17], which are not yet fully understood in terms of basic reaction-diffusion models of CO oxidation. It is believed that, in this regime, additional transport processes (gas phase coupling [46]) and different absorption states (subsurface oxygen [47,48]) play a crucial role, thus requiring an extension of present models of the reaction.

A. Large domains

We started by confirming that in sufficiently large domains (e.g., 500×500 μm^2) the surface indeed reproduces the patterns observed on the macroscopic crystal, as well as in polycrystalline samples with grain sizes of a few hundred micrometers [21]. Figure 3 shows the abbreviation FHI for the Fritz-Haber-Institut [Fig. 3(a)] and the Princeton "shield" [Fig. 3(b)]. These are comparatively large domains (the overall diameter is ≈350 μm).

The surrounding Ti-covered surface is inactive and shows no pattern formation. In the shield one can see spiral waves of different wavelengths developing. The formation of spiral waves is frequently observed and has been well investigated on the Pt(110) surface [20,49]. In the narrow (20 μm width) channels at the sides of the sign, reaction-diffusion pulses propagate. This highlights one of the advantages of the microstructured geometrical domains we are using: by making one of the two dimensions of the domain small (here, by using narrow, quasi-one-dimensional channels), we can study the effect of *dimensionality* on certain instabilities and patterns [44,50]. In this case, two-dimensional spirals become wave trains in the narrow channels.

A similar picture appears on the FHI sign. In this case we point out the coexistence of multiple "states" under the same operating conditions: while the F and the I are uniformly covered, the H shows the formation of spirals turning into wave trains in its long, straight channels. Worth noting are the effects of diffusion anisotropy both in the shape of the fronts and especially in the way they go around corners; notice how the fronts detach from the left vertical and into the horizontal bar of the H; the fronts follow a small scratch at the top of the left leg of the H.

Figure 4 contains another sequence in the Princeton shield that demonstrates both the transition from two to one dimensional, but also some boundary effects. In the narrow channels of the Princeton shield an oxygen front approaches a CO front and they form a stable pulse. The formation of pulses from interacting fronts in bi-

stable systems has been predicted (e.g., by Rinzel and Terman [51]), but had so far not been directly seen in an experiment. The so formed pulse, upon exiting the channel [see the arrow in Fig. 4(g)], tries initially to remain normal to both boundaries. Because, however, spirals are not yet stable in two dimensions, it detaches from the left-hand-side boundary (the one with the abrupt corner) and shrinks and disappears following the right-hand-side boundary. This indicates a parameter regime where pulses are stable, but spirals are not. Such a regime would be very difficult to detect on an open catalyst surface.

The dynamics of the interaction between two rival spirals in a large domain are shown in Fig. 5. The scenario starts with three spirals coexisting at the top of the shield: the one on the left has a longer rotation period and wavelength, while the ones on the right are separated by a scratch (marked in the figure). The lower

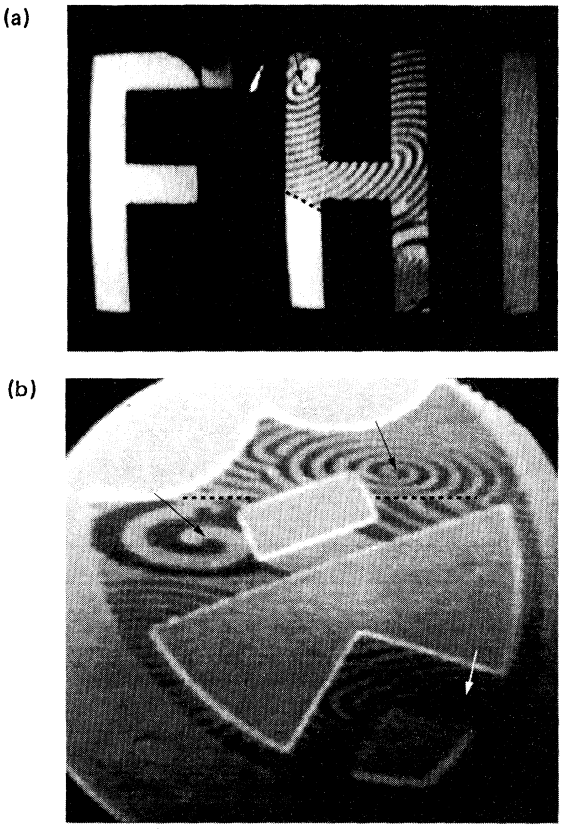

FIG. 3. Examples of large domain patterns: (a) three letter-shaped domains at $p_{CO}=5.0\times10^{-5}$ mbar, $p_{O_2}=4.0\times10^{-4}$ mbar, and $T=440$ K. While the middle one exhibits spiral and periodic wave trains, the left and the right domains are uniformly covered. Spiral cores are marked by arrows, while the location of a scratch is highlighted with a dashed black line. (b) shows a domain in the shape of the Princeton shield with several spiral waves (their tips are marked by arrows) and a large scratch (also marked by a dashed black line). The conditions are $p_{CO}=3.15\times10^{-5}$ mbar, $p_{O_2}=4.0\times10^{-4}$ mbar, and $T=446$ K. Both the letters and the Princeton shield are 350 μm high.

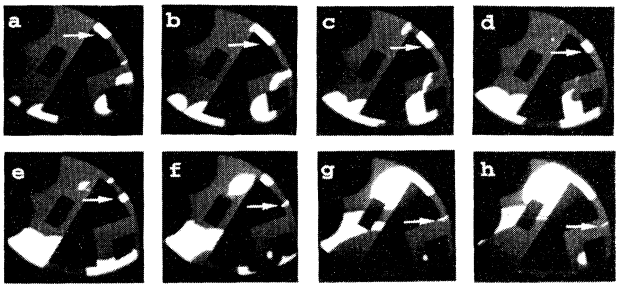

FIG. 4. A sequence in the Princeton shield at conditions in the regime where fronts dominate on the open surface ($p_{CO}=3.05\times10^{-5}$ mbar, $p_{O_2}=4.0\times10^{-4}$ mbar, and $T=446$ K). A pair of fronts, marked by the white arrow, forms a pulse in the small channel at the right-hand side of the shield. Upon exiting this channel, the pulse dies by shrinking. The time interval between the pictures is 15 s for frames $a-g$ and 4 s between frames g and h. The size of the shield is the same as in Fig. 3(b).

of these two right-hand-side spirals communicates through parallel waves with the domain of the fatter one on the left, which is pinned at a defect; eventually the latter is taken over and the location of the pinning of the left-hand side spiral's core is indicated by the imperfection (see the arrow) in Fig. 5(b). This picture is in complete agreement with the observations and simulations of spiral competition by Nettesheim *et al.* [20] and Bär *et al.* [49].

Figure 5(c) shows the pattern after an increase in CO pressure. The lower of the two right-hand-side spirals tried to take on a larger core size. Its tip then ran into the boundary and the spiral was destroyed. Lacking this competition, the left-hand-side spiral pinned to the large

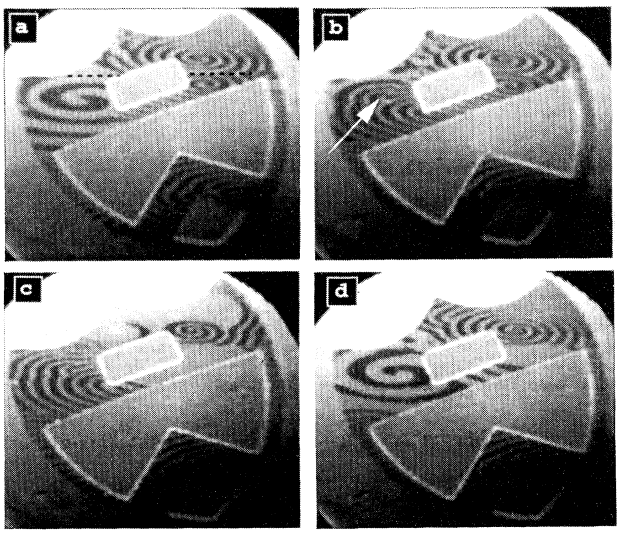

FIG. 5. Subsequent stages of interaction of spirals with each other and with the boundaries in the Princeton shield. The conditions are identical to Fig. 3(b), except that $p_{CO}=3.10\times10^{-5}$ mbar in (a) and (b). A slight change of p_{CO} to 3.15×10^{-5} mbar happens between (b) and (c) and causes the death of the lower spiral of the right-hand-side pair. Again, the scratch is marked with a dashed black line in (a).

defect reappears [Fig. 5(d)]. The last picture also demonstrates that the right-hand-side spiral pair in Figs. 5(a) and 5(b) was separated by the large scratch: in Fig. 5(d) the waves from the upper right remaining spiral do not penetrate the lower right region. While there is more to this spiral competition scenario in the shield, and while the boundaries of these large domains do interact significantly with the fate of the concentration waves and the ultimate observable picture, they do not play an active role in the basic pattern selection as long as the spirals' center of rotation is sufficiently far away from the boundary.

B. Dynamics of an isolated defect

The catalytic surface, even though it is a polished single crystal, can be quite nonuniform. In addition to atomic scale lattice defects such as steps and terraces, there also exist mesoscopic defects (very often scratches and other imperfections) at a scale that dramatically interacts with spatiotemporal pattern formation. A simple way of rationalizing these defects is as *inhomogeneities* of the surface: locations with different properties, i.e., locations where the effective parameter values are different from those of the surrounding surface. It is thus possible, for example, to talk of a small, predominantly CO-covered defect on an otherwise oxygen-covered surface and vice versa. Under certain (excitable) conditions, such a defect might be able to emit concentration waves of CO (O) into the O-covered (CO-covered) surface. A second possibility (in reaction-diffusion terminology) is given by an oscillatory defect in an otherwise excitable surface. Defects can provide nucleation sites for fronts and pulses and pinning sites for spiral waves and may often act as pacemakers for the remaining surface.

Because we can construct small reactive regions, it is often possible to isolate a single surface defect and study its intrinsic dynamics and their interplay with pattern formation. It is also possible to study small regions that apparently do *not* contain defects and thus elucidate the inherent chemical dynamics of the surface. Figure 6 shows the persistent oscillations of a small (20×20 μm^2) square: they consist of a periodic firing, originating at a location in the upper left of the square. To a first level of description, an elliptic white (CO) front starts at that location, followed by a dark (oxygen) front; this implies the existence of an unresolvable and thus unobservable defect at this location. The fronts propagate over the surface, which then uniformly returns to its previous state until the defect fires again. Figure 7 confirms the periodicity of the phenomenon: the rate of firing remains essentially constant in time for fixed operating conditions.

Closer inspection of additional data indicates something more interesting about the nature of the oscillation in small oxygen-covered domains. Apparently each firing consists of two steps: first comes a fast, light front, which starts at the defect and quickly covers the free surface; this is followed by a slower, darker front (the one we first identified), which starts at the same defect and also covers the surface; the cycle is repeated after some time.

This two-step version of front firing has been consistently observed in many different geometries and for several different operating conditions. Figure 8 shows its occurrence in a circular geometry. There exists also an interesting variation on the same theme in some of the data: the two fronts, which still occur in the same order, can originate at different locations in the geometry. Finally, it is worth noting that under some conditions it is possible for the second front to start *before* the first one has exited the domain. Under such conditions, the two fronts may catch up with each other forming a pulse. It should be mentioned that while the whole sequence of waves presented in Fig. 8 lasts only a few seconds, the time to the next firing event is much longer (≈ 17 s).

A careful study of the rate of firing vs operating condi-

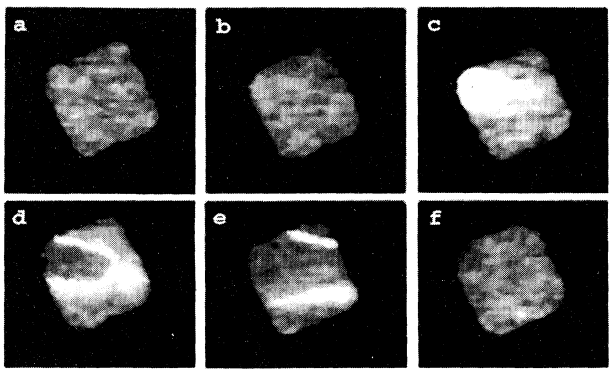

FIG. 6. Pulselike CO waves on a 20×20 μm^2 square. The conditions are $p_{CO}=1.3\times10^{-4}$ mbar, $p_{O_2}=4.0\times10^{-4}$ mbar, and $T=570$ K. The time interval between pictures is 0.2 s.

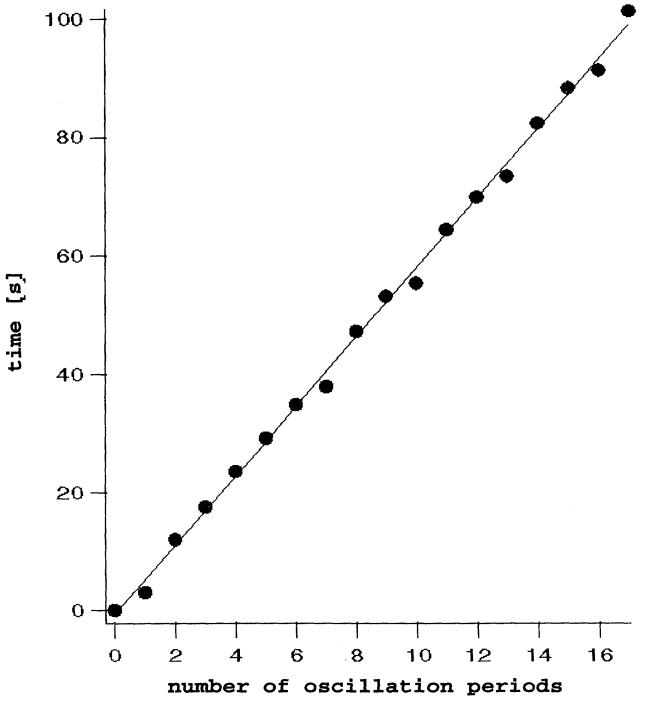

FIG. 7. Number of CO pulse induced oscillations on the square in Fig. 6 (and identical conditions) as a function of time.

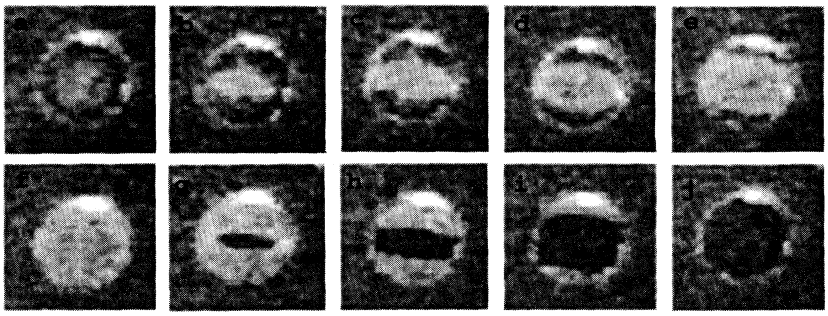

FIG. 8. A two-step event of fronts [a light one in (a) is followed by a dark one in (g)] in a circular geometry with diameter 60 μm. The control parameters are $p_{CO}=9.8\times10^{-5}$ mbar, $p_{O_2}=4.0\times10^{-4}$ mbar, and $T=488$ K. The time interval between frames is 0.25 s.

tions shows that (at a constant temperature of 488 K) the period of the oscillation increases dramatically from 7 to 71 s as the CO pressure decreases from 1 to 0.9×10^{-4} mbar. For CO pressures below the latter value, the firing of the defects stopped and the small domain remained permanently in an oxygen covered state. This type of information might be interpreted as a variation of the refractory time (i.e., the minimum time between two pulses) in an *excitable* (oxygen-covered) medium upon a CO pressure change.

We constructed a two-dimensional array of several hundred 10×10 μm^2 separate reacting squares in order to obtain some statistics on the dynamics of comparable domains; in this experimental regime the coupling between these domains through the gas phase is believed to be very weak. We observed that, for $p_{CO}=2.0\times10^{-4}$ mbar, $p_{O_2}=6.0\times10^{-4}$ mbar, and $T=560$ K, the squares are oscillating with periods varying between 1 and 2 s. It is tempting to assume that the rate of oscillations of each square depends on the size (or type) of the defect(s) contained in the square, possibly on the *number* of such defects. In this case, the observed behavior is more driven by the existence of active defects rather than by the geometry and size of the reacting domain *per se*. It has been a general observation that, in these experiments, a larger domain is more likely to exhibit patterns than a small one. In light of the above observations, a likely reason for this is simple probability: the larger a domain, the more likely it is to contain an active defect that can initiate front motions.

C. One-dimensional patterns

By constructing domains with one dimension that is small relative to the characteristic pattern size, it is possible to constrain the patterns to be effectively one dimensional. Figure 9 shows, in a sequence of snapshots, the progression of a single CO pulse in a ring (7.5 μm thickness, 40 μm outer diameter). This is a paradigm of reaction-diffusion patterns in an *anisotropic* medium: the shape and the speed of the pulse change depending on its angle with respect to the crystallographic axes. The ratio of the wave speeds along the different crystal orientations of the surface is roughly 1:2, implying a ratio of 1:4 between diffusion coefficients (since the wave speed is proportional to the square root of the diffusion coefficient). This ratio is also reflected by the evolution of the pulse length (shown in Fig. 10). The axis for faster diffusion is indicated by the arrow in Fig. 10(b). Notice that the curvatures of the leading edge and the trailing edge of the pulse are different. The pulse travels around in about 40 s and it persisted for CO partial pressure changes of up to 5%. This pulse was stable for many minutes. The small defect indicated by the arrow in Fig. 9(d) has no significant influence on the pulse. The light inner circle in Fig. 9 is predominantly CO-covered Pt, separated from the ring we described above by 5 μm of Ti. The overall micropattern was composed of several concentric rings, the next one of which is partly visible in the figure, also uniformly covered by CO.

This case shows how a simple controlled geometry isolates a canonical pattern: a single traveling pulse. In addition, it brings to light the anisotropy, one of the unique aspects of reactions on single crystal surfaces. A simulation of this phenomenon is presented below in Sec. IV. In experiments on larger rings, we have found that transient pulses will break as they curve around the ring, especially at the transition from slow to fast diffusion: apparently the CO pulses detach from one of the two boundaries and subsequently die or become islands of CO attached to the

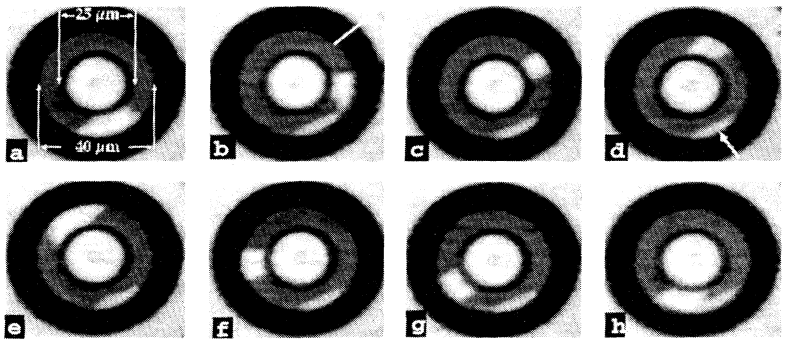

FIG. 9. Isolated CO pulse on a ring at $T=469$ K, $p_{CO}=1.3\times10^{-4}$ mbar, and $p_{O_2}=4.0\times10^{-4}$ mbar. The time interval between frames is 5 s. The white arrow in (b) marks the fast diffusion direction.

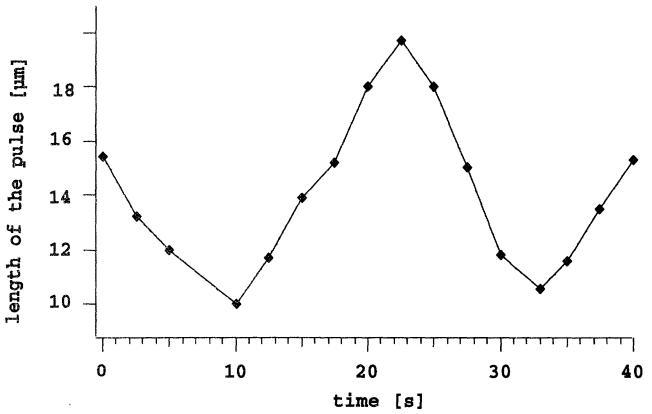

FIG. 10. Variation of the length of the pulse in Fig. 9 with time during roughly 80% of a full rotation.

other boundary, interacting with subsequent traveling pulses.

In uniform simple excitable or bistable media (with only the activator diffusing), a front, once formed, does not change direction. Nevertheless, in our experiments we repeatedly observed cases where fronts *did* reverse their direction either in the interior of an apparently uniform domain or at a boundary (scratch). Figure 11 shows a domain composed of a number of channels placed parallel to each other. A scratch transects the upper set of channels and CO fronts initiate (and remain pinned) at both sides of that scratch. These CO fronts move in an apparently undecided fashion back and forth in the channels, changing directions for no apparent reason, and sometimes returning all the way back to the scratch where they originated. When, however, they grow long enough to reach the opposite boundary of the channel, they never again retreat and a predominantly CO-covered steady state prevails.

A similar configuration is shown in Fig. 12: a sequence of nested circular arcs as formed by a set of rings transected by an almost diametrical scratch; this scratch is visible as a horizontal dark line at the top of the panels. As the sequence of images shows, fronts are formed in one of these arcs at the boundary scratch and they subsequently travel back and forth, reversing themselves into oxygen fronts at a defect visible around the "seven o'clock" position in the arc. A related observation in the same geometry is shown in Fig. 13: the right front recedes from the defect towards the boundary [an oxygen front, marked with a black arrow in Fig. 13(b)] as the left front (CO, marked with a light arrow) travels from the boundary towards the defect.

While in the latter example front reversal can be attributed to the presence of a defect, in the case of parallel channels above, front reversal "for no apparent reason" is an interesting phenomenon, because it is not *a priori* clear how it can arise from the interplay between reaction and diffusion on a homogeneous surface under constant external conditions. A potential explanation is that the reaction was operated at conditions close to a so-called front bifurcation, where small, otherwise unimportant fluctuations in surface properties or external conditions might trigger a transition from a CO front branch to an oxygen front branch, as was stipulated in recent theoretical investigations with the FitzHugh-Nagumo model [14,15]. In the case of reversal at scratch and/or defect boundaries, it is not known whether simple reaction-diffusion systems are capable of reproducing the phenomenon for some choice of altered kinetics and/or boundary conditions representative of the scratch.

A related quasi-one-dimensional pattern is shown in Fig. 14. In this "synchrotron" a pulse traveling down the inlet splits into two pulses traveling in opposite directions in the ring. Usually, the two pulses annihilate upon collision. Here their behavior is different: as they reach the other side of the ring, they run into a defect (a scratch) growing back from both sides towards the entrance of the ring. The existence of a CO front argues for bistability under these conditions. This defect-induced change in the interaction of pulses bears some similarity to the solitonlike behavior of pulses on the excitable, CO-covered surface [52]. The narrowness of the channels, as stated at the beginning, plays an important role in making these phenomena observable. As we will see below, large channels and curvatures result in strong two-dimensional effects that can destroy quasi-one-dimensional pulses.

Another typical interaction of a quasi-one-dimensional phenomenon with a boundary is shown in Fig. 15. A CO

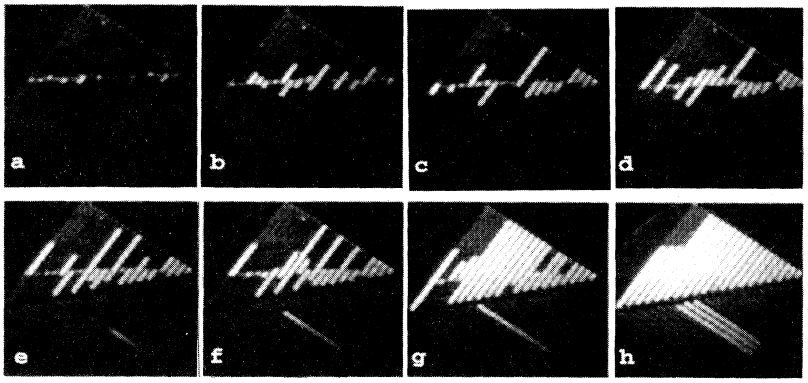

FIG. 11. Waves moving in small channels of different length and orientation at $p_{CO} = 2.3 \times 10^{-5}$ mbar, $p_{O_2} = 4.0 \times 10^{-4}$ mbar, and $T = 420$ K. The channel width is 20 μm and the time interval between pictures is 2 min.

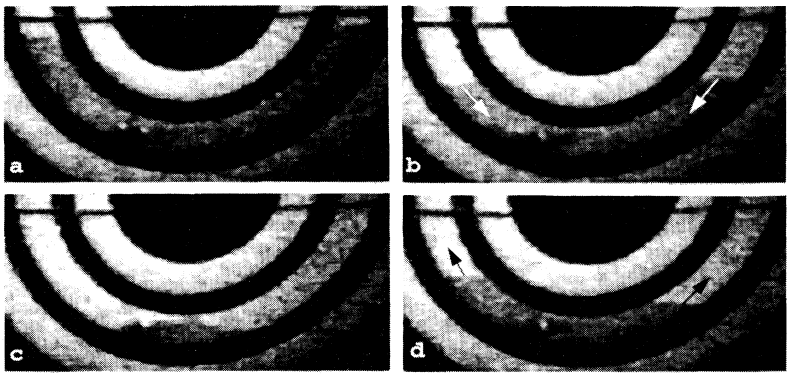

FIG. 12. Front oscillation in a ring segment. Propagating CO fronts are marked by white arrows, oxygen fronts by black ones. The fronts are reflected at the boundaries and at the defect in the segment (visible as a black dot at the seven o'clock position). The conditions are $p_{CO}=1.15\times10^{-4}$ mbar, $p_{O_2}=4.0\times10^{-4}$ mbar, and $T=511$ K. The time interval between pictures is ≈2 s and the radius of the ring is 50 μm.

pulse is interrupted by running into a solid object (the parallelogram at the top of the Princeton shield; it travels around it on both sides and tries to remain normal to its boundary on both sides. When the (opposite-traveling) fronts meet on the back of the obstruction, they pinch off in a cusp, which becomes gradually smoother, and the pulse practically heals itself. This healing process can be used to measure the diffusion coefficient in the medium (see [41,53]).

Figure 16 shows the interaction of a front with a sudden expansion. The spiral in the first frame died through interaction with the boundary due to a change in operating conditions. The 100-μm-diam circle surface was completely covered by CO and a CO front entered and slowly moved up the bottleneck connected with the circle [Fig. 16(b)]. This CO front eventually reaches the scratch [marked by an arrow in Fig. 16(a)]; upon reaching it, it immediately reverts in a dark oxygen front, which swiftly moves in the reverse direction down the bottleneck. This oxygen front exits the small channel and eventually fills the circular bottle. In this case, the oxygen front appears elliptic in shape [Figs. 16(e) and 16(f)]. Depending on the orientation of dumbbell-shaped domains we constructed, pulses traveling through the neck connecting two circular regions may exit this neck completely parallel or they may curve significantly to elliptic shapes.

The passage of a pulse through a door is shown in the sequence of Fig. 17. The geometry consists of two hexagonal domains coupled through an opening on their common side. The CO pulse originates in the bottom of the right-hand hexagon, it approaches the opening, and it goes through it. It then turns around following the lower part of the boundary, thus creating the beginning of a swirl: the original front continues moving upwards, while its edge has started to move downward. By being normal to the boundary on both sides, it eventually breaks into two antiparallel pulses, one traveling towards the top and one towards the bottom of the left-hand hexagon.

D. Effect of a grid of inert islands

This section deals with an attempt at a geometry incorporating a large number of features: a catalytic domain where the boundaries participate more actively in pattern selection. We deposited on the surface a regular grid of inert titanium pillars; this grid is a square array of ~10-μm-wide Ti "islands" with a lattice constant of ~20 μm. The experiments on the grid were initiated at low CO pressures with a completely oxygen covered surface. Upon an increase of p_{CO}, the system enters the parameter regime where coexisting fronts are observed (compare with Fig. 2). Pattern formation then starts with CO fronts, initiated at a scratch that divides the lattice into two subdomains. At a somewhat higher value of CO pressure, these fronts and the oxygen fronts following them start to form stable pulses and spiral waves of CO on an oxygen-covered (black) background. The spirals that first appear tend to be pinned to the islands of the inert lattice. An example is shown in Fig. 18.

There is another reason for including this sequence: it shows a spiral wave that alternatively rotates counterclockwise and clockwise. In the sequence, one wave is pinned to the circle marked with the cross and is turning

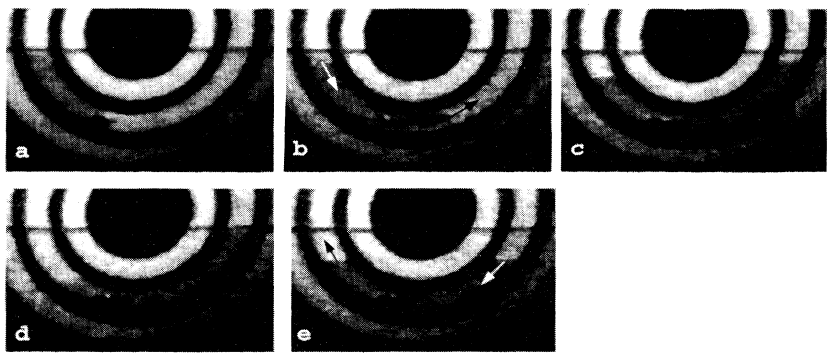

FIG. 13. Same geometry and conditions as in Fig. 12. Now the bouncing mode is no longer symmetric around the defect, i.e., the fronts on the left- and the right-hand sides of the ring segment are out of phase. The time interval between pictures is ≈2 s.

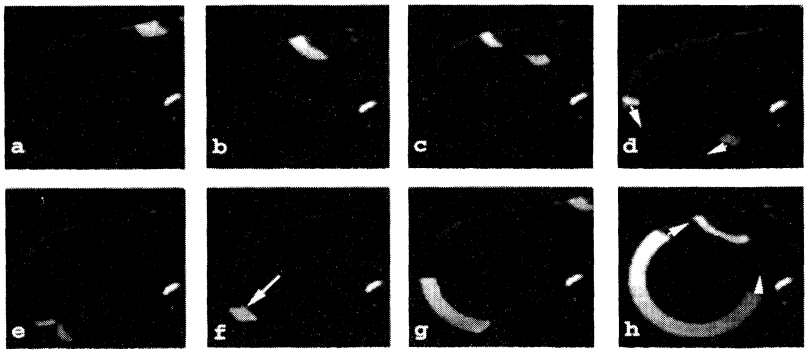

FIG. 14. A CO pulse moves into a synchrotonlike geometry and splits in two. The resulting pulses collide in the ring and are reversed at a defect marked by an arrow in frame *f*. The reversed waves are CO fronts. The control parameters are $p_{CO}=4.6\times10^{-5}$ mbar, $p_{O_2}=4.0\times10^{-4}$ mbar, and $T=470$ K. The picture size is 150×150 μm^2 and the time interval between frames is roughly 20 s.

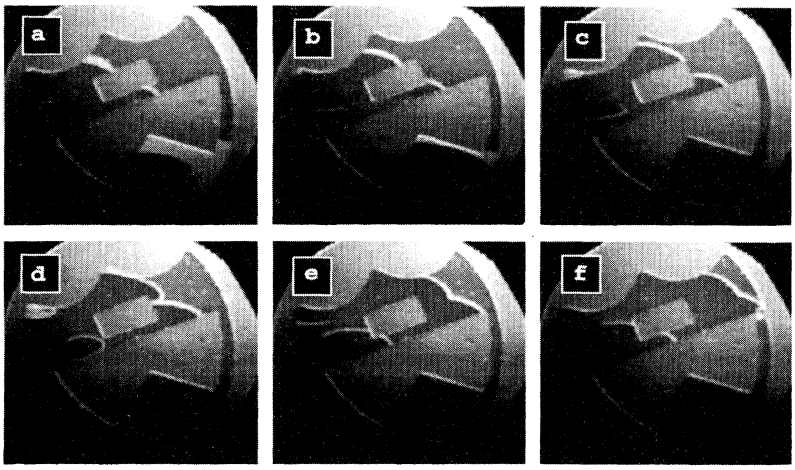

FIG. 15. A CO pulse (white) moving from left to right in the upper part of the Princeton shield is interrupted by a square obstruction. The conditions are $p_{CO}=4.44\times10^{-5}$ mbar, $p_{O_2}=4.0\times10^{-4}$ mbar, and $T=447$ K. The time interval between frames is 5 s and the height of the shield is 350 μm.

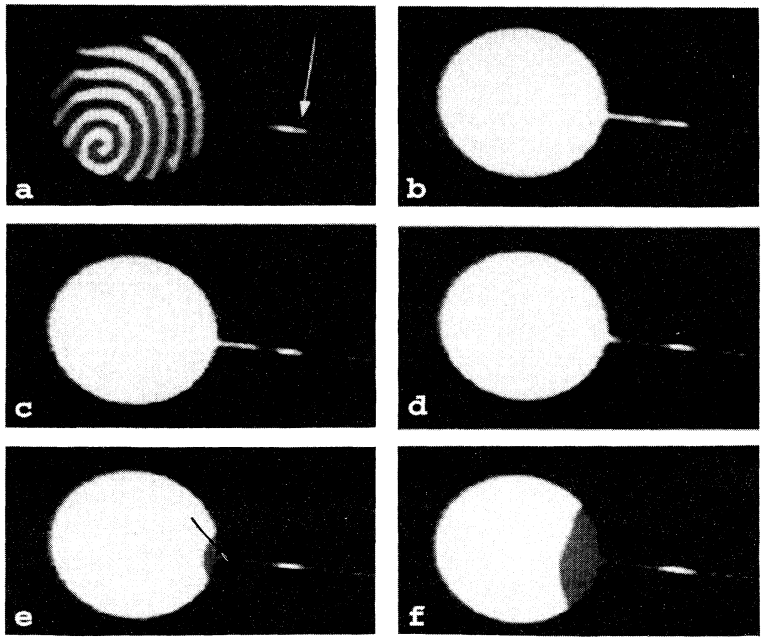

FIG. 16. After the spiral in (a) died due to a change in CO pressure, a CO front moves down the narrow channel and is finally blocked by a scratch marked by an arrow in (a). Finally, an oxygen front originates from the same defect, propagates inward, and fills the circular domain. The conditions are $p_{CO}=3.6\times10^{-5}$ mbar, $p_{O_2}=4.0\times10^{-4}$ mbar, and $T=432$ K. The diameter of the circle is 100 μm.

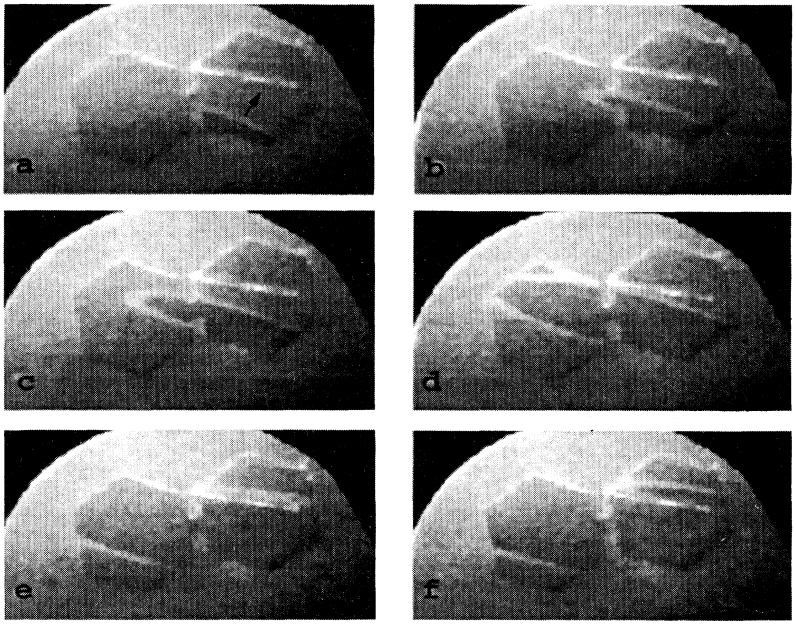

FIG. 17. A pulse starts at the bottom of the right hexagon and moves through the opening into the left hexagon. The parameters are $p_{CO}=1.08\times10^{-4}$ mbar, $p_{O_2}=4.0\times10^{-4}$ mbar, and $T=489$ K. The height of the hexagons is 100 μm and the time interval between frames is 1.5 s.

counterclockwise. In Fig. 18(c) one end of the front hits the next Ti spot and, as can be seen in Fig. 18(d), sticks to it. Now the front is pinned to both Ti circles and starts to turn clockwise at the top one, although it is still turning counterclockwise at the lower, initial pinning point. In Fig. 18(g) the front finally tears apart and there remain two spirals with different rotational direction, pinned on different Ti islands. Note that through this process, a wavelength is produced that is comparable to the lattice spacing.

A further increase in CO pressure led to the appearance of unpinned, *free* spirals inside the grid [see the left arrow in Fig. 19(a)]. These spirals had considerably shorter wavelength (10 μm) and period. In contrast to the pinned spirals, these spirals start to fill the entire grid with the pulses they emit. Figure 19 shows four successive snapshots of the interaction of such a family of pulses with the inert grid. Locally, one can see the beginnings of multiarmed spirals pinned on the Ti islands [notice the four-armed spiral marked with the right arrow in Fig. 19(a)]. As a rotating arms of the spirals encounter the rows of Ti islands, the lattice tends to slow down and flatten the pulses by forcing them to become short arcs connected at cusps. Such a pulse [see the one in between the arrows in Fig. 19(a)] while moving parallel to the grid deforms and heals itself between successive rows of obstructions.

In all these pictures, the average distance between fronts appears somehow commensurate to the lattice spacing; as a matter of fact, one can extract a roughly 2:1 ratio in the horizontal direction and a comparable ratio in the vertical direction. It should be noted that the grid axes are not aligned with (they actually are at an approximately 45° angle to) the principal axes of diffusion of the crystal. This phenomenon of average spatiotemporal resonance between the front spacing and the grid has been repeatedly observed and is probably caused by the substantial delay in the propagation of waves between grid points. It appears that various degrees of order on a grid-covered domain are associated with various types of spirals: pinned spirals, with one up to four arms, and "free" spirals, which do not rotate around one of the grid

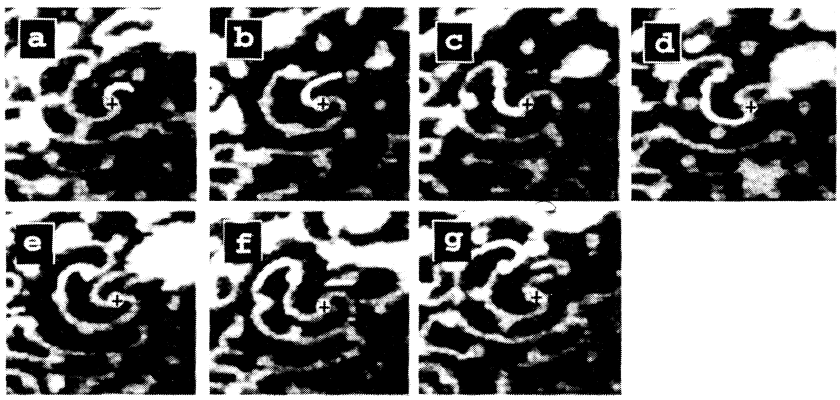

FIG. 18. The pinned spiral rotates counterclockwise around a grid element (marked with a cross) and becomes attached to a second element, where it rotates clockwise. The conditions are $p_{CO}=2.4\times10^{-5}$ mbar, $p_{O_2}=4.0\times10^{-4}$ mbar, and $T=425$ K. The distance between the grid elements is 20 μm.

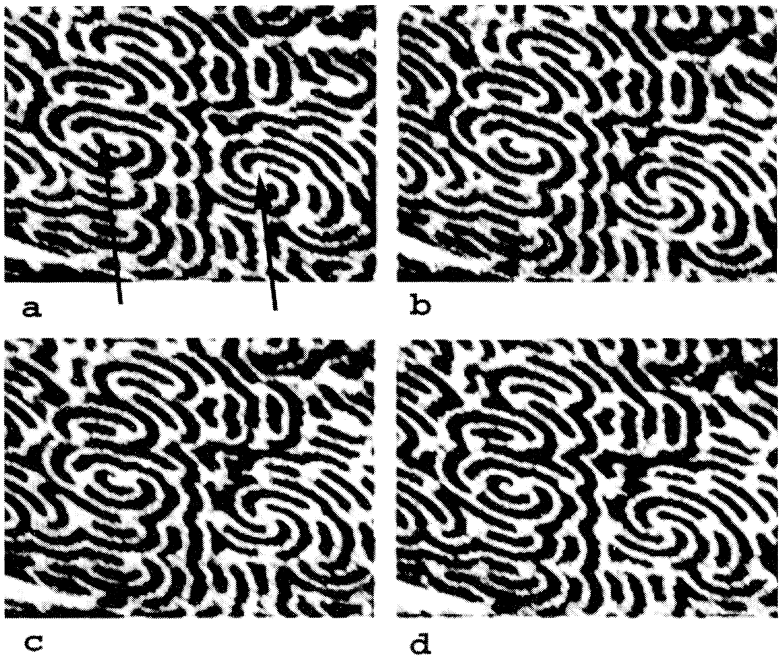

FIG. 19. Wave pattern in the grid created by a free spiral (left arrow) and a multiarmed spiral (right arrow). The conditions are $p_{CO}=2.4\times10^{-5}$ mbar, $p_{O_2}=4.0\times10^{-4}$ mbar, and $T=425$ K. The distance between the grid elements is 20 μm and the time between two frames is 30 s.

elements (but might be associated with some other, unresolved defect). This is one of the subjects we consider in the simulation section below. It is worth noting that under certain conditions the grid plays apparently no role in the pattern formation. Such a case is shown in Fig. 20, where solitary oxygen pulses travel without apparent interaction with the grid; the normal to these pulses denotes the direction of slow diffusion along the crystal (the [001] axis), thus showing the relative orientation of the crystal and the grid.

E. Effects of subsurface oxygen

Under certain conditions, very bright regions have been observed by the PEEM. These regions have a work function approximately 1 eV smaller than that of the pure surface and have been interpreted as a new "species": oxygen that has penetrated the surface layer, so-called *subsurface* oxygen [47,48,54].

Figure 21 shows a CO front propagating upwards towards the Ti boundary of a Pt circle (a CO front appears as the boundary between the light gray and the dark, oxygen-rich areas, and propagates into the oxygen rich region). Subsurface oxygen (bright) appears first in Fig. 21(c), starting as a thin line at the CO front boundary, and is possibly formed from the surface oxygen between the front and the wall. When the remaining oxygen covered area becomes smaller, its work function decreases even more. This might be due to a higher concentration of subsurface oxygen [Figs. 21(d) and 21(e)]. Finally, it rebounds, emitting a dark oxygen front consisting of chemisorbed surface oxygen [Figs. 21(f) and 21(g)]. An interesting quirk of the crystal made this a periodic phenomenon: the downward moving front bounces off an oblique scratch transecting the domain near the position of the front in Fig. 21(h). So the oxygen front turns again into a CO front and the procedure repeats itself stably

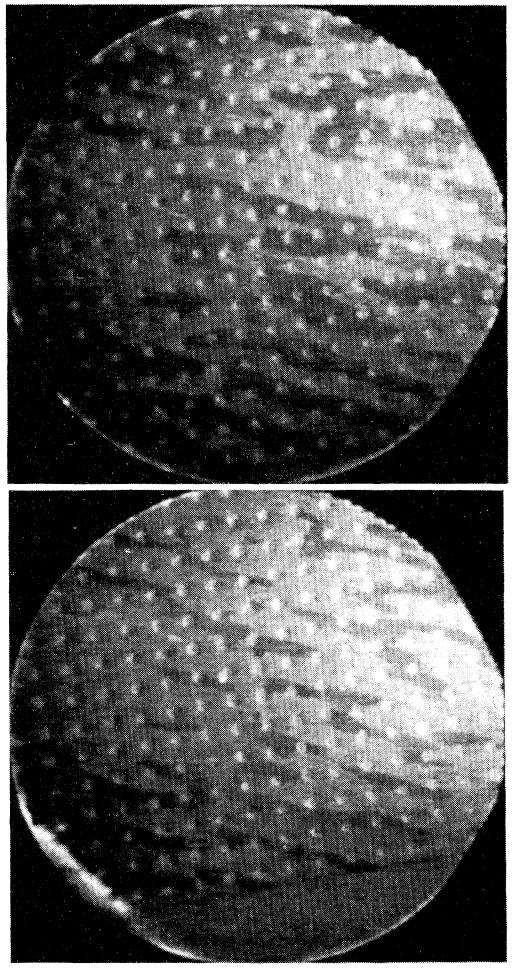

FIG. 20. Examples of solitary-wave-like patterns in the grid. The conditions for both pictures are $p_{CO}=9.7\times10^{-5}$ mbar, $p_{O_2}=4.0\times10^{-4}$ mbar, and $T=485$ K.

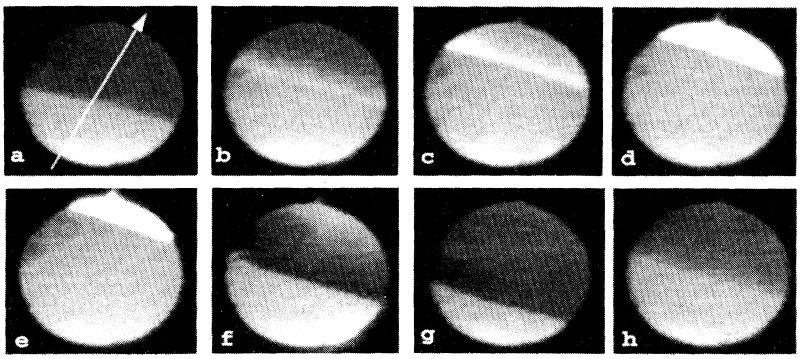

FIG. 21. "Bouncing" of fronts in a circular domain. The bright areas at the top of (d) and (e) indicate the formation of subsurface oxygen. The control parameters are $p_{CO}=2.4\times10^{-5}$ mbar, $p_{O_2}=4.0\times10^{-4}$ mbar, and $T=457$ K. The diameter of the circular domain is 100 μm.

with a period of ~2 min. This periodic production and removal of subsurface oxygen was observed for many minutes under fixed conditions. The conversion of chemisorbed oxygen atoms with a high work function to the subsurface species is also visible in the corresponding intensity profiles (Fig. 22), taken along the white arrow marked in Fig. 21(a). In this case, the gray scale level of the clean surface in the arbitrary units of Fig. 22 is approximately equal to 21, that of chemisorbed oxygen is 10, and that of CO is around 19. Subsurface oxygen has a maximum level of 25, much brighter than the clean surface. On untreated samples, subsurface oxygen is often formed when two, opposite-moving CO fronts "squeeze" the oxygen-covered surface between them; on the microstructured crystal only a single CO front moving towards a wall boundary is seen to cause this effect. In many instances, the neighborhood of inert Ti boundaries appears to assist the formation of subsurface oxygen; we saw ample evidence of this in the Ti grid as well as close to domain corners.

Figure 23 shows another example, where the bright species (i.e., subsurface oxygen) was flickering around a defect like a candle flame, exhibiting a stable period of about 2 s. The rest of the surface was homogeneously covered with CO and no dark oxygen waves were observed. We have also observed bright species pulses, formed at the interface between two CO colliding fronts in a circular arc.

These examples are cases where artificial boundaries allow us to isolate, observe, and explore a new step in the mechanism of CO oxidation, the formation of subsurface oxygen. Subsurface oxygen has been already proposed in 1982 as a possible mechanism for kinetic oscillations in the CO oxidation at atmospheric pressures by Sales, Turner, and Maples [55]; however, it has not yet been included in models for the CO oxidation on Pt single crystal surfaces under low pressure conditions; nevertheless, for certain conditions, it may play a significant role in the nature of the instabilities and patterns found in this reaction.

IV. THEORY

To put the experimental results in perspective, we present here a brief discussion of the current state of the theory for the CO oxidation reaction on Pt. It proceeds via a Langmuir-Hinshelwood mechanism [56,57]:

$$CO_{gas}+* \rightleftharpoons CO_{ad} ,$$

$$O_{2,gas}+2* \rightarrow 2O_{ad} ,$$

$$CO_{ad}+O_{ad} \rightarrow CO_{2,gas}+2* ,$$

where * denotes an unoccupied site on the surface and the subscripts ad (gas) represent the adsorbed (gaseous) form of CO and oxygen.

In addition, the clean Pt(110) surface reconstructs in the 1×2 "missing row" structure, which is lifted at sufficiently high concentrations of adsorbed CO [58]. Based on experimental evidence about the individual reaction steps, a model for the *temporal* behavior was developed in terms of a set of ordinary differential equations, which reproduces well much of the experimental observations such as bistability and the onset of kinetic oscillations of the overall reaction rate, depending on the external control parameters [59–62].

In order to describe the formation and the properties of spatiotemporal patterns, this model was extended into a set of partial differential equations by including surface diffusion of adsorbed CO (which exhibits much higher mobility than adsorbed oxygen atoms). Here we start with a simplified two-variable version of this model [49], which reads in dimensionless units

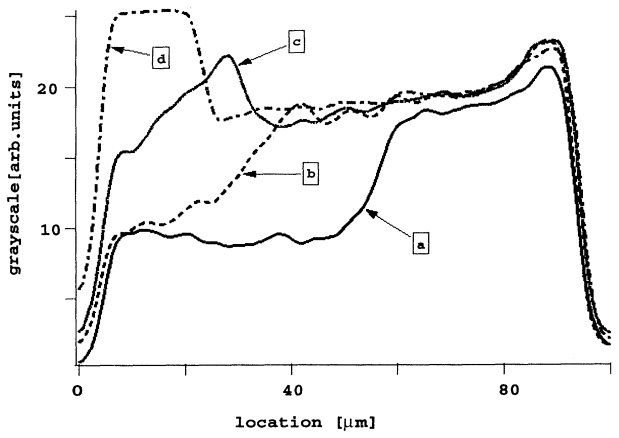

FIG. 22. Intensity profiles for Figs. 21(a)–21(d); shown is the image brightness along the white line in Fig. 21(a).

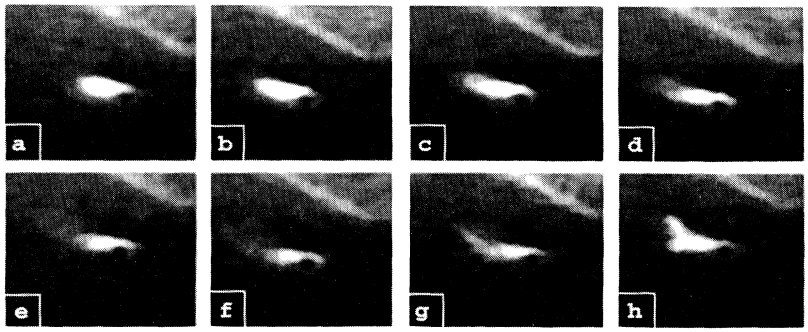

FIG. 23. Flamelike behavior of subsurface oxygen (white) on a CO-covered surface (dark gray). The conditions are $p_{CO}=7.9\times10^{-5}$ mbar, $p_{O_2}=4.0\times10^{-4}$ mbar, and $T=522$ K. The picture size is 50×45 μm^2.

$$\frac{\partial u}{\partial t}=\nabla^2 u+\frac{1}{\epsilon}u(1-u)[u-u_{th}(w)]\ , \tag{1}$$

$$\frac{\partial w}{\partial t}=f(u)-w\ , \tag{2}$$

where u is a measure of the surface coverage, w the surface structure, and $u_{th}(w)=(w+b)/a$. Note that $u=0$ corresponds to a CO (O) coverage of 0.65 (0.001) ML and that $u=1$ represents 0.2 ML CO (0.25 ML O) on the Pt surface. One space (time) unit in Eq. (1) [(2)] is for the experimental conditions presented above of the order of 1 μm (1 s). The interested reader might consult [49] for a detailed description of the scaling procedure. The function $f(u)$ gives the dependence of the surface structure on the amount of CO coverage and was fitted from experimental data [61]. The model calculations here are carried out under excitable conditions, for which $f(u)$ is taken to be

$$f(u)=\begin{cases}0 & \text{if } u<\frac{1}{3}\\ 1-6.75u(u-1)^2 & \text{if } \frac{1}{3}\le u\le 1\\ 1 & \text{if } u>1\ .\end{cases} \tag{3}$$

Equations (1)–(3) resemble a generic model of excitable media introduced by Barkley and his co-workers [63,64] for fast efficient numerical simulation in the excitable regime. A specific difference from Barkley's model can be seen in the form of $f(u)$. The standard choice $f(u)=u$, used in many models of excitable media [8], is here replaced by a more complicated form, which can be interpreted as a delayed inhibitor w production. This delay leads to phenomena such as spiral breakup and backfiring of solitary pulses [65], which had not been found in classical excitable media. The simulations here are carried out in the range of conditions where an extended surface shows stable spirals and pulses. The parameter values ($a=0.84, \epsilon=0.025$, and $b=0.07$) were adapted to typical experiment conditions ($T=450$ K, $p_{O_2}=4.0\times10^{-4}$ mbar, and $p_{CO}=4.3\times10^{-5}$ mbar; see also [20,49]).

Another specific property of the Pt(110) surface is the anisotropic diffusion, which to a first approximation is captured by a symmetric, positive-definite diffusion tensor. For an anisotropic system, the diffusion term must be slightly modified; the Laplacian term in Eq. (1) is replaced by

$$\nabla\cdot\mathbf{D}\cdot\nabla u\ ,$$

where $\mathbf{D}$ is a symmetric positive-definite constant diffusivity tensor. We consider the simple case

$$\mathbf{D}=\begin{bmatrix}D_x & 0\\ 0 & D_y\end{bmatrix}=\begin{bmatrix}1 & 0\\ 0 & 0.25\end{bmatrix}\ ,$$

where D_x and D_y are diffusion coefficients in the x and y directions, respectively. On an open surface this anisotropy is usually scaled out by a suitable stretching of the spatial coordinate, thus recovering equations of the form (1) and (2). The typical ratio between the length scales is 1:2, implying a 1:4 ratio D_x/D_y of the diffusion constants (the diagonal entries in the diffusion coefficient tensor, corresponding to diffusion rates along the crystal principal axes). For systems with nontrivial boundary geometries, this procedure no longer applies, since the appropriate length transformation would also change the shape of the boundary and thus the problem.

Here we present simulations confined to a few of those experimental situations that exhibit a decisive influence of the boundary conditions on the pattern formation, namely, the circulating pulse in a quasi-one-dimensional circular ring and the interaction of waves with the inert grid (cf. Figs. 9, 18, and 19). The simulations of the ring were carried out with a finite difference version of the anisotropic Laplacian in polar coordinates, exploiting the natural symmetry of the problem. The computational scheme was supplemented by periodic boundary conditions in the angular direction and by zero-flux conditions in the radial direction. They can in principle also be done (and were done for Barkley's model) in a Cartesian square grid, but this requires special treatment of the boundary layer and limits the time step due to the irregular small distances (compared to the grid constant) between the outer grid points and the boundary [66].

The numerical results of a rotating pulse in a ring, which are displayed in Fig. 24, clearly show a strong influence of the anisotropy of the diffusion, in accordance with the experimental observations. Note that the ring used in the simulation has a considerably smaller diameter than the one in the experiment of Fig. 9, thus allowing for higher numerical accuracy through finer spatial and temporal resolution. However, simulations with larger rings revealed essentially the same qualitative features as described below. The front accelerates and curves when

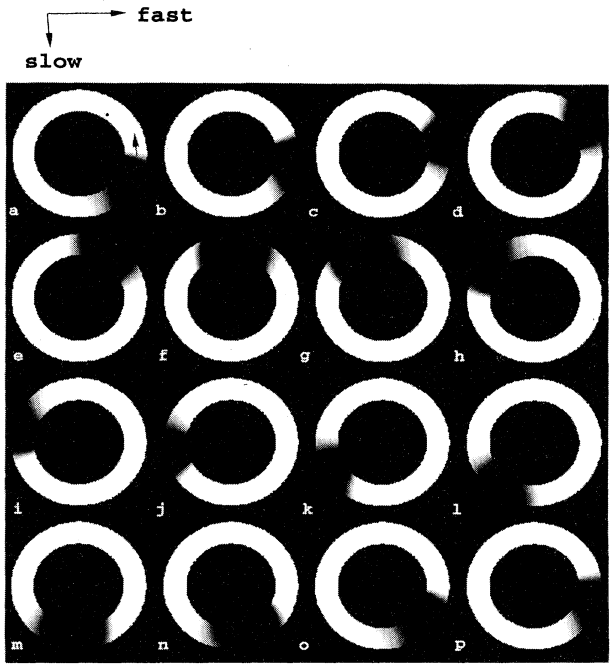

FIG. 24. Simulation of a pulse in a ring with model equations (1)–(3) under excitable conditions ($a=0.84$, $b=0.07$, and $\epsilon=0.025$). The width of the ring is 1.5 space units, the inner (outer) radius is 3.0 (4.5). We used 30 mesh points in the radial direction and 400 mesh points in the angular direction. The time interval between pictures is 0.66. One space unit corresponds to 1.2 μm and a time unit to 2 s for $T=450$ K.

its path aligns with the fast diffusion direction and it slows down when moving along the slow diffusion direction. When the pulse moves fast, there is a considerable difference between the curvatures of the front and the back of the pulse. It is interesting to consider the relative motion of the inner versus the outer contact of the pulse with the domain walls. While the inner end of the pulse, which has to travel an overall shorter distance, precedes the outer end as the circular arc curves from the faster towards the slower diffusion direction, the outer end of the pulse accelerates and even overtakes it when the path curves from the slower to the faster diffusion direction.

The effect, although less pronounced, occurred also in the experiments. In contrast, it was absent in simulations with isotropic diffusion. It can be traced back to the interplay of the circular boundary and the anisotropic diffusion: Consider that the inner end of the pulse (the one attached to the inner boundary) is more advanced when it enters the slow propagation direction; the normal to the pulse at its outer boundary still points towards the faster diffusion direction. Thus the outer end will accelerate, temporarily become faster, and will be able to catch up or possibly overtake the inner end. In the next arc segment (when the domain curves from the slower to the faster direction) the effect will be reversed. Note that the orientation of the inner and the outer ends of the pulse (which are different for the front and the back of the pulse) are affected by the zero-flux condition at the boundary.

To quantify the described phenomenon, we extracted the wave velocity of the pulse during its rotation at different positions of the ring, namely, at its inner and outer boundaries. This was achieved by dividing the whole ring in 40 segments and detecting the entry and the exit of the pulse into each segment. In the case of a medium with isotropic diffusion, the angular velocity is independent of the rotation angle; the absolute linear velocity is, naturally, proportional to the radial distance from the center of the ring. This behavior can be rationalized by the curvature dependence of the wave velocity in excitable media [67]

$$c(K)=c(0)-D_n K \ ,$$

i.e., different parts of the pulse travel with different velocities $c(K)$ due to a variation in curvature (K); D_n is the diffusion coefficient locally normal to the wave. It should be kept in mind that the above relation is valid only for weakly curved fronts (here for a sufficiently larger inner radius of the ring) and media with dominant activator diffusion (here CO diffusion). The results for the pulse in a ring with *isotropic* diffusion indicated negative (positive) curvature of the wave at the outer (inner) boundary (consistent with the pulse's constant shape and the linear distances the two ends have to travel). The velocities for a pulse rotating in a ring with *anisotropic* diffusion strongly depend on the local angle of its position with the principal diffusion axes as shown in Fig. 25. For a periodic geometry such as the ring, speed variations are, of course, locked to the rotation of the pulse. Here the difference in traveling distance for different parts of the pulse were additionally compensated for by a further mechanism: the variation (during a revolution) of the velocity at the outer boundary was much smaller than that at the inner boundary. Thus the average velocity at the outer edge was considerably higher. As described above, this can be explained by taking into account the orientation of the forefront of the pulse towards the principal axes of diffusion *in addition to* the curvature effects already present in iso-

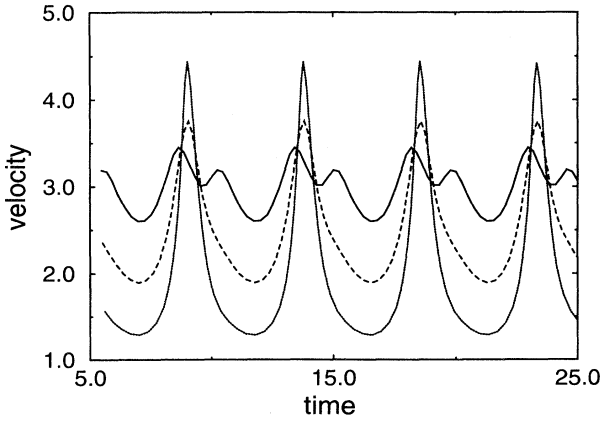

FIG. 25. Variation of the velocity of the pulse shown in Fig. 24 during two full rotations of the pulse. The full, dashed, and dotted lines represent the velocity at the outer boundary, in the middle of the ring, and at the inner boundary, respectively. A velocity unit corresponds to 0.6 μm s^{-1}, a time unit to 2 s.

tropic systems. An interesting feature of Fig. 25 is the "double hump" oscillation of the speed of the outer end of the pulse forefront, which signals the overtaking of the inner by the outer end of the wave front.

The detailed behavior of the pulse depends on the ratio between the inner and the outer radius of the ring boundary. Suppose the inner ring shrinks to a smaller radius r_1 (or the outer one grows). Then one expects a transition to a spiral wave pattern at the limit $r_2 - r_1 \gg 2\pi r_1$. In that case the rotating pulse "unwinds" to a spiral whose core is pinned to the inner ring. The relation between a rotating pulse and a pinned spiral remains an interesting point to be studied further in experiments and model calculations.

The second example we study through simulations is the interaction of waves with an inert rectangular grid. For computational simplicity we consider the grid to consist of little squares instead of circles (the pattern on the photolithography mask indeed consisted of squares, which, however, became slightly rounded by the etching process). In addition, the computational grid axes are aligned with the diffusion principal axes; the experimental grid was not well aligned with the crystallographic axes. The computations were done with the Cartesian version of the Laplacian operator. To provide a suitably complex initial condition, a state with many (~ 80) spirals was created by a simulation of the unbounded surface in the "turbulent" regime ($\epsilon = 0.075$). The inert defects (zero-flux boundaries) were subsequently introduced and the actual simulations were performed at $\epsilon = 0.025$, where without the regular grid individual spirals would persist and form a complex pattern with oscillatory dynamics. We also assumed a scratch at the upper horizontal boundary with constant oxygen coverage, which acts as a wave source upon the excitable, CO-rich state. The grid has the ability to pin spirals and thus change the overall dynamics. The degree of this change depends on the lattice spacing as well as on the size of the grid elements (squares or circles). A typical scenario, which comes close to the experimental observations at $T = 425$ K (Fig. 19), is shown in Fig. 26. Only a few of the starting population of free spirals persist. Many of the others got pinned and were eventually suppressed by the higher-frequency free ones. This leads to a high degree of coherence in the pattern.

If the lattice constant is substantially increased, the influence of the grid on the pattern practically vanishes [Fig. 27(a)]. This figure was obtained from the same initial condition as Fig. 26 after the same evolution time. The same phenomenon occurs when the size of the grid elements is made considerably smaller without changing the lattice constant [Fig. 27(b)].

A higher density of grid points lead to a different pattern [Fig. 27(c)]: here free spirals can no longer be supported in the narrow spacing between grid elements and the grid is eventually filled by periodic waves both from a pinned spiral and from the wave source at the top. Note that the evolution time in this example was about ten times longer than in the other cases. For completeness, Fig. 27(d) gives the enlarged final state of the simulation presented in Fig. 26, for comparison with the other pictures.

To conclude, an inert grid is likely to alter pattern formation by pinning one or more spiral arms to a single grid element. The simulations reveal that with increasing grid density and element size, the number of free spirals decreases. Thus the coherence of the pattern will become more pronounced. All in all, the introduction of a grid provides for an extensive length of boundary per domain area and thus enhances and selects patterns favored by the existence of nearby boundaries (as opposed to open surface patterns). This may result in dramatic differences in pattern selection and we are in the process of investigating the effects of both regular and random grids of various symmetries, both inert and active (i.e., composed of different metals, such as Au or Pd).

The model we used here has been capable of qualitatively reproducing several of the observed open surface

FIG. 26. Simulation of the evolution of waves in a grid with Eqs. (1)–(3), starting from a "turbulent" initial condition containing many spiral wave seeds. The conditions are excitable ($a = 0.84$, $b = 0.07$, and $\epsilon = 0.025$). The time interval between frames is 3.93 and the domain size is 100×100. 256×256 mesh points are used for the integration. The grid elements are squares with a side length of 2.74 and a lattice spacing of 5.94. One space unit corresponds to 1.2 μm and a time unit to 2 s for $T = 450$ K.

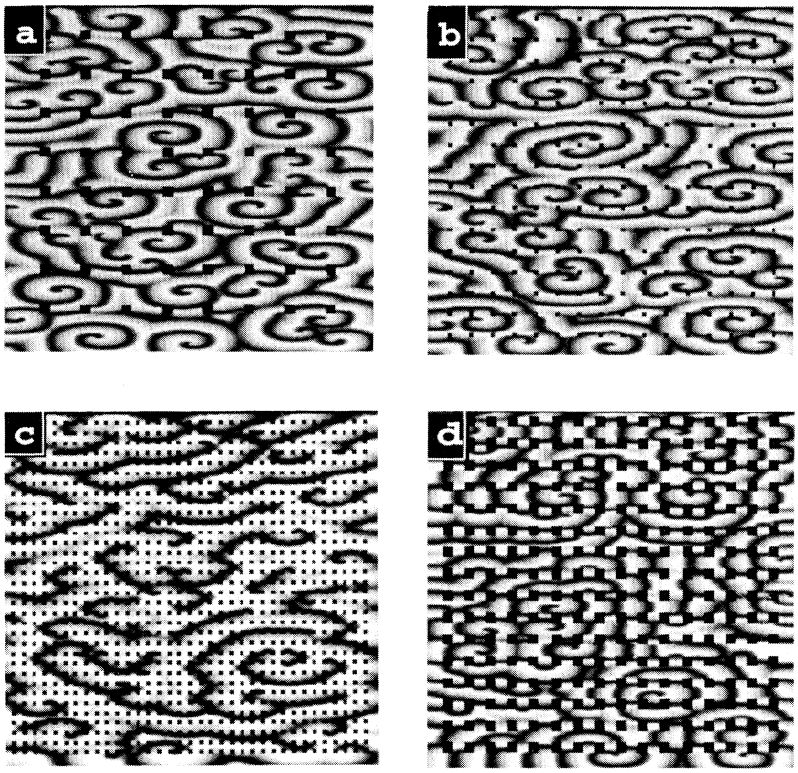

FIG. 27. Wave configurations for varying lattice spacings and element sizes. The parameters and the initial conditions of the integration are identical to Fig. 26. The integration time is 61.5 in (a), (b), and (d) and 615 in (c). (a) The lattice spacing is 10.98 and the square size is 2.74×2.74. (b) The lattice spacing is 5.94 and the square size is 1.18×1.18. (c) The lattice spacing is 2.74 and the square size is 1.18×1.18. (d) The lattice spacing is 5.94 and the square size is 5.94×5.94. One space unit corresponds to 1.2 μm and a time unit to 2 s for $T=450$ K.

phenomena such as solitary-type pulses, front propagation, and spiral patterns [49,52,68]. With the inclusion of appropriate boundary conditions in the present work, this model has also reproduced phenomena we have observed on microstructured surfaces. It is, however, also evident that a number of effects still have to be incorporated in the model. A fundamental issue is the effective modeling of anisotropy. The diffusivity actually depends on the surface state (degree of reconstruction as well as surface local coverage) in a way that has been demonstrated recently [69]. The speed and the shape of the isolated pulse in a ring should provide an excellent paradigm for quantitative comparison of theory and experimental results.

In addition, the formation of subsurface oxygen is not yet contained in the model. The significance of this species becomes clear in our experiments, particularly in the examples of Sec. III E. In the meantime, experimental results about the formation of subsurface oxygen are becoming available, which should provide the data necessary to explain the formation mechanism [48]. Hence the model might also be extended in order to reproduce the observed bouncing and "flaming" motions described above.

V. CONCLUSION AND HIGHLIGHTS

The construction of microstructured catalytic surfaces enabled us to study catalytic reactions in domains of controlled size and shape. This approach has allowed us to examine individual elements of the surface dynamics. It set the stage for a number of dynamic interactions between the domain geometry and the spontaneous pattern formation. It also highlighted the interplay between crystal anisotropy and boundary geometry. Finally, it revealed a number of effects that had not been previously observed in experiments nor predicted by modeling. The setting developed here permits the systematic study of pattern formation *per se,* as well as its interactions with domain geometry. Simple prototype experiments should motivate quantitative comparisons between kinetic model building, simulations, and experimental work.

Here we used photolithography to pattern the surface. In a similar spirit, a submonolayer coating of Au was evaporated onto the surface through a mask and CO oxidation on this modified surface has already revealed promising initial results [70]. Photolithography has also been used to construct *active* palladium boundaries on a Pt(110) surface, since Pd also catalyzes the reaction. Sputtering of the Pd "pillars" reduced them to monolayer or submonolayer thickness domains surrounded by Pt, over which the reactants could also diffuse. It is obvious that a large class of inhomogeneous composite catalysts with regular or irregular (but controlled) geometry can be constructed with such techniques. Other microfabrication and nanofabrication techniques (such as ion beam epitaxy) can be used for the same purpose. In particular, we plan to create patterns not by building inert walls between them, but separating them with ditches plowed using an scanning-tunneling microscope head. These ditches can be used to simulate the effect of scratches on the surface, changing both its transport and reaction properties. They can be made at prescribed angles to the crystallographic axes and, depending on their size, they

can provide a range of boundary conditions for the reacting domains. In the experiments we reported here, the pacemakers for surface activity were often imperfections and inhomogeneities (scratches, defects) of the surface. The firing rate of these defects was observable and could change with operating conditions, but could not be changed at will. A promising research direction would be to construct microscopic pacemakers (to begin with, small localized heating elements) that would initiate pulses and fronts based on controlled external stimuli.

The phenomena observed on the microdesigned catalyst often were different from those obtained on the bare catalyst at the same conditions and depended on the size and the shape of the domain. This approach may provide a systematic way to alter and possibly actively control the overall properties (reaction rate, conversion, selectivity) for some surface reactions.

ACKNOWLEDGMENTS

The authors thank Professor Steve Forrest and Mike Lange for sample preparation and Dwight Barkley for the use of his EZ–SPIRAL code for simulating excitable media. This work was partially supported through ARPA/ONR, the National Science Foundation, the Deutsche Forschungsgemeinschaft, and the Alexander von Humboldt Foundation. M. B. and I. G. K. would also like to acknowledge the hospitality of the Center for Nonlinear Studies (CNLS) at Los Alamos National Laboratory.

[1] A. S. Mikhailov, *Foundations of Synergetics* (Springer-Verlag, Berlin, 1990).
[2] M. C. Cross and P. C. Hohenberg, Rev. Mod. Phys. **65**, 851 (1993).
[3] A. M. Turing, Philos. Trans. R. Soc. London B **237**, 37 (1952).
[4] V. Castets, E. Dulos, J. Boissonade, and P. de Kepper, Phys. Rev. Lett. **64**, 2953 (1990).
[5] Q. Ouyang and H. L. Swinney, Nature **352**, 610 (1991).
[6] *Oscillations and Traveling Waves in Chemical Systems,* edited by R. J. Field and M. Burger (Wiley, New York, 1985).
[7] J. Ross, S. C. Müller, and C. Vidal, Science **240**, 460 (1988).
[8] A. T. Winfree, Chaos **1**, 303 (1991).
[9] G. Ertl, Science **254**, 1750 (1991).
[10] Y. Kuramoto, *Chemical Oscillations, Waves and Turbulence* (Springer-Verlag, Berlin, 1984).
[11] Q. Ouyang and H. L. Swinney, Chaos **1**, 411 (1991).
[12] K. J. Lee, W. D. McCormick, Q. Ouyang, and H. L. Swinney, Science **261**, 192 (1993).
[13] J. E. Pearson, Science **261**, 189 (1993).
[14] A. Hagberg and E. Meron, Phys. Rev. Lett. **72**, 2494 (1994).
[15] A. Hagberg and E. Meron, Chaos **4**, 477 (1994).
[16] H. H. Rotermund, W. Engel, M. Kordesch, and G. Ertl, Nature **343**, 355 (1990).
[17] S. Jakubith, H. H. Rotermund, W. Engel, A. von Oertzen, and G. Ertl, Phys. Rev. Lett. **65**, 3013 (1990).
[18] H. H. Rotermund, S. Jakubith, A. von Oertzen, and G. Ertl, Phys. Rev. Lett. **66**, 3083 (1991).
[19] H. H. Rotermund, Surf. Sci. **283**, 87 (1993).
[20] S. Nettesheim, A. von Oertzen, H. H. Rotermund, and G. Ertl, J. Chem. Phys. **98**, 9977 (1993).
[21] J. Lauterbach, G. Haas, H. H. Rotermund, and G. Ertl, Surf. Sci. **294**, 116 (1993).
[22] W. Engel, M. E. Kordesch, H.-H. Rotermund, S. Kubala, and A. von Oertzen, Ultramicroscopy **36**, 148 (1991).
[23] Z. Noszticzius, W. Horsthemke, W. D. McCormick, H. L. Swinney, and W. Y. Tam, Nature **329**, 619 (1987).
[24] W. Y. Tam and H. L. Swinney, Physica D **46**, 10 (1990).
[25] G. Philippou, F. Schultz, and D. Luss, J. Chem. Phys. **95**, 3224 (1991).
[26] S. L. Lane and D. Luss, Phys. Rev. Lett. **70**, 830 (1993).
[27] M. D. Graham, S. L. Lane, and D. Luss, J. Phys. Chem. **97**, 7564 (1993).
[28] G. A. Cordonier and L. D. Schmidt, Chem. Eng. Sci. **44**, 1983 (1989).
[29] H. Linde and C. Zirkel, Z. Phys. Chem. **174**, 145 (1991).
[30] H. Linde and H. Engel, Physica D **49**, 13 (1991).
[31] A. M. Zhabotinsky, M. D. Eager, and I. R. Epstein, Phys. Rev. Lett. **71**, 1526 (1993).
[32] A. Toth, V. Gaspar, and K. Showalter, J. Phys. Chem. **98**, 522 (1994).
[33] I. Zuburtikudis and H. Saltsburg, Science **258**, 1337 (1992).
[34] A. M. Pertsov, E. A. Ermakova, and E. E. Shnol, Physica D **44**, 178 (1990).
[35] J. Enderlein, Phys. Lett. A **156**, 429 (1991).
[36] A. Babloyantz and J. A. Sepulchre, Physica D **49**, 52 (1991).
[37] B. Y. Kogan, W. J. Karplus, B. S. Billett, and W. G. Stevenson, Physica D **59**, 275 (1992).
[38] J. A. Selpuchre and A. Babloyantz, Phys. Rev. E **48**, 187 (1993).
[39] K. Agladze, J. P. Keener, S. C. Müller, and A. Panfilov, Science **264**, 1746 (1994).
[40] M. D. Graham, I. G. Kevrekidis, K. Asakura, J. Lauterbach, K. Krischer, H.-H. Rotermund, and G. Ertl, Science **264**, 80 (1994).
[41] S. Nettesheim, Ph.D. thesis, Freie Universität Berlin, 1993 (unpublished).
[42] P. Ortoleva and J. Ross, J. Chem. Phys. **63**, 3398 (1975).
[43] Ch. Zülicke, A. S. Mikhailov, and L. Schimansky-Geier, Physica A **163**, 559 (1990).
[44] A. Hagberg and E. Meron, Phys. Rev. E **48**, 705 (1993).
[45] M. Bär, S. Nettesheim, H.-H. Rotermund, M. Eiswirth, and G. Ertl, Phys. Rev. Lett. **74**, 1246 (1995).
[46] M. Eiswirth, P. Möller, K. Wetzl, R. Imbihl, and G. Ertl, J. Chem. Phys. **90**, 510 (1989).
[47] H. H. Rotermund, J. Lauterbach, and G. Haas, Appl. Phys. A **57**, 507 (1993).
[48] J. Lauterbach, K. Asakura, and H.H. Rotermund, Surf. Sci. **313**, 52 (1994).
[49] M. Bär, N. Gottschalk, M. Eiswirth, and G. Ertl, J. Chem. Phys. **100**, 1202 (1994).
[50] M. Kness, L. S. Tuckerman, and D. Barkley, Phys. Rev. A **46**, 5054 (1992).
[51] J. Rinzel and D. Terman, SIAM J. Appl. Math. **42**, 1111 (1982).
[52] M. Bär, M. Eiswirth, H. H. Rotermund, and G. Ertl, Phys. Rev. Lett. **69**, 945 (1992).

[53] P. Förster, S. C. Müller, and B. Hess, Science **241**, 685 (1988).
[54] J. Lauterbach, Ph.D. thesis, Freie Universität Berlin, 1994 (unpublished).
[55] B. C. Sales, J. E. Turner, and M. B. Maple, Surf. Sci. **114**, 381 (1982).
[56] T. Engel and G. Ertl, Adv. Catalysis **28**, 1 (1979).
[57] R. P. H. Gasser, *An Introduction to Chemisorption and Catalysis by Metals* (Clarendon, Oxford, 1985).
[58] T. Gritsch, D. Coulman, R. J. Behm, and G. Ertl, Phys. Rev. Lett. **63**, 1086 (1989).
[59] R. M. Eiswirth, K. Krischer, and G. Ertl, Appl. Phys. A **51**, 79 (1990).
[60] K. Krischer, M. Eiswirth, and G. Ertl, Surf. Sci. **251/252**, 900 (1991).
[61] K. Krischer, M. Eiswirth, and G. Ertl, J. Chem. Phys. **96**, 9161 (1992).
[62] K. Krischer, M. Eiswirth, and G. Ertl, J. Chem. Phys. **97**, 303 (1992).
[63] D. Barkley, M. Kness, and L. S. Tuckerman, Phys. Rev. A **42**, 2489 (1990).
[64] D. Barkley, Physica D **49**, 61 (1991).
[65] M. Bär and M. Eiswirth, Phys. Rev. E **48**, R1635 (1993).
[66] W. Ames, *Numerical Methods for Partial Differential Equations* (Academic, New York, 1977).
[67] J. J. Tyson and J. P. Keener, Physica D **32**, 327 (1988).
[68] M. Falcke, M. Bär, H. Engel, and M. Eiswirth, J. Chem. Phys. **97**, 4555 (1992).
[69] A. von Oertzen, H.-H. Rotermund, and S. Nettesheim, Surf. Sci. **311**, 322 (1994).
[70] K. Asakura, J. Lauterbach, H. H. Rotermund, and G. Ertl, Phys. Rev. B **50**, 8043 (1994).

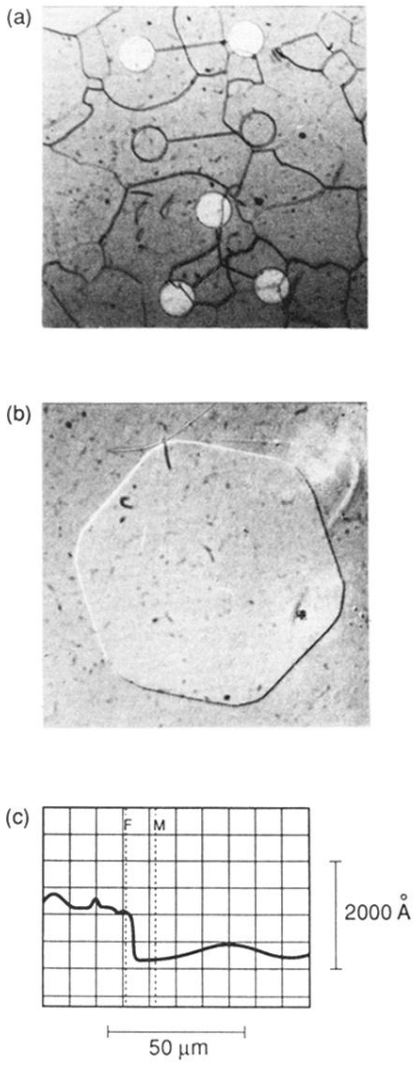

FIG. 1. Photographs of the treated Pt surfaces: (a) dumbell- and three-lobed dumbell-shaped domains on the polycrystalline sample (the picture size is $800 \times 800\ \mu m^2$ and the dark lines are the grains boundaries) and (b) hexagonal domain on the Pt(110) single crystal surface (the picture size is $225 \times 225\ \mu m^2$). (c) shows a depth profile across a domain boundary. The titanium layer is to the left, the pure Pt surface to the right.

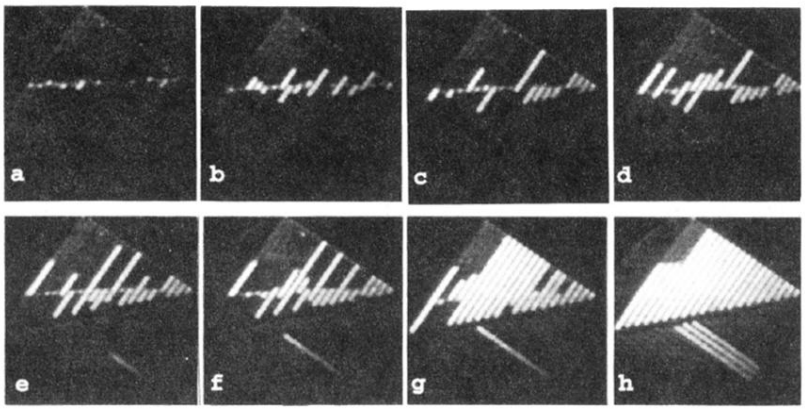

FIG. 11. Waves moving in small channels of different length and orientation at $p_{CO}=2.3\times10^{-5}$ mbar, $p_{O_2}=4.0\times10^{-4}$ mbar, and $T=420$ K. The channel width is 20 μm and the time interval between pictures is 2 min.

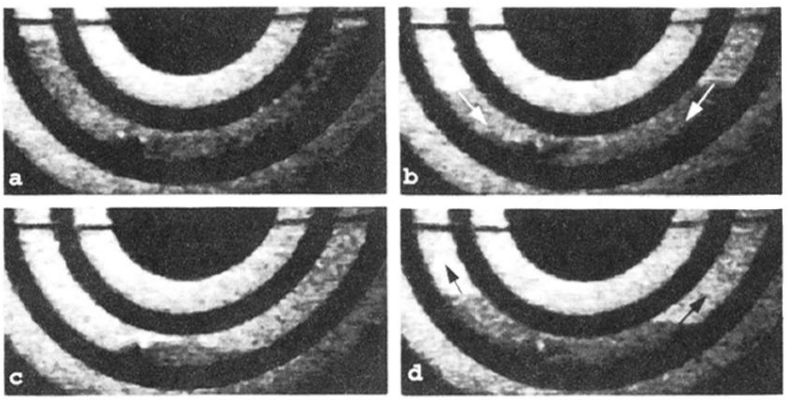

FIG. 12. Front oscillation in a ring segment. Propagating CO fronts are marked by white arrows, oxygen fronts by black ones. The fronts are reflected at the boundaries and at the defect in the segment (visible as a black dot at the seven o'clock position). The conditions are $p_{CO}=1.15\times10^{-4}$ mbar, $p_{O_2}=4.0\times10^{-4}$ mbar, and $T=511$ K. The time interval between pictures is ≈ 2 s and the radius of the ring is 50 μm.

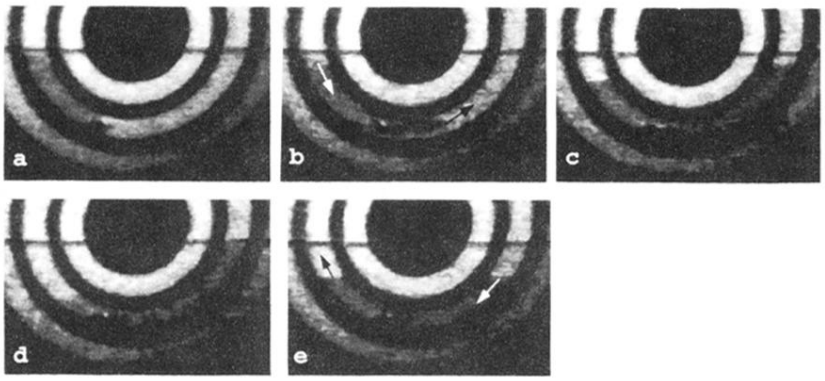

FIG. 13. Same geometry and conditions as in Fig. 12. Now the bouncing mode is no longer symmetric around the defect, i.e., the fronts on the left- and the right-hand sides of the ring segment are out of phase. The time interval between pictures is ≈ 2 s.

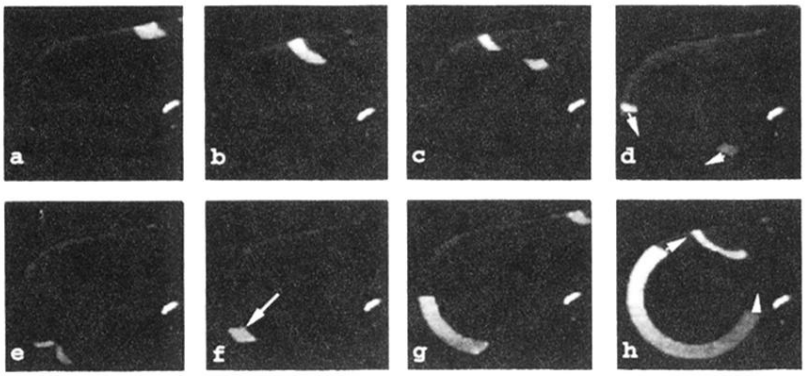

FIG. 14. A CO pulse moves into a synchrotonlike geometry and splits in two. The resulting pulses collide in the ring and are reversed at a defect marked by an arrow in frame *f*. The reversed waves are CO fronts. The control parameters are $p_{CO}=4.6\times10^{-5}$ mbar, $p_{O_2}=4.0\times10^{-4}$ mbar, and $T=470$ K. The picture size is 150×150 μm^2 and the time interval between frames is roughly 20 s.

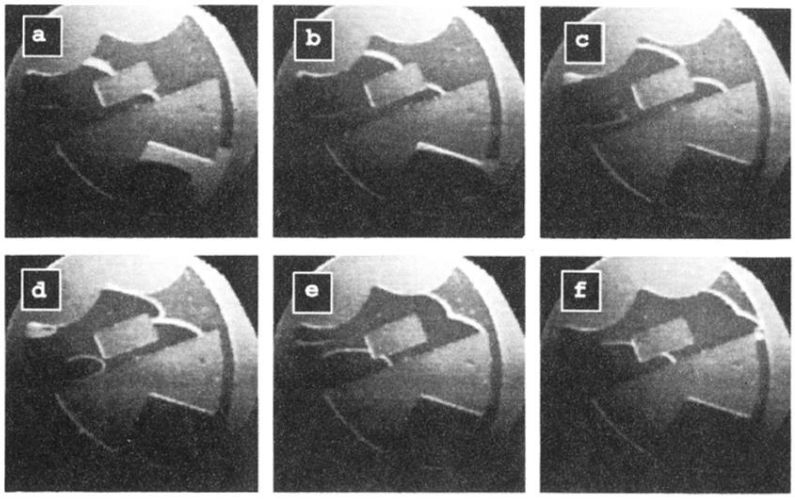

FIG. 15. A CO pulse (white) moving from left to right in the upper part of the Princeton shield is interrupted by a square obstruction. The conditions are $p_{CO}=4.44\times10^{-5}$ mbar, $p_{O_2}=4.0\times10^{-4}$ mbar, and $T=447$ K. The time interval between frames is 5 s and the height of the shield is 350 μm.

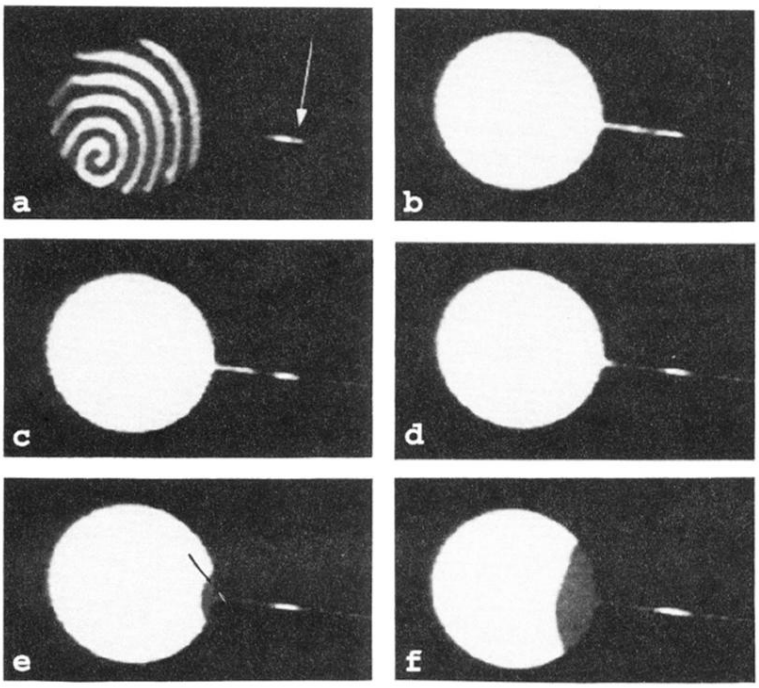

FIG. 16. After the spiral in (a) died due to a change in CO pressure, a CO front moves down the narrow channel and is finally blocked by a scratch marked by an arrow in (a). Finally, an oxygen front originates from the same defect, propagates inward, and fills the circular domain. The conditions are $p_{CO}=3.6\times10^{-5}$ mbar, $p_{O_2}=4.0\times10^{-4}$ mbar, and $T=432$ K. The diameter of the circle is 100 μm.

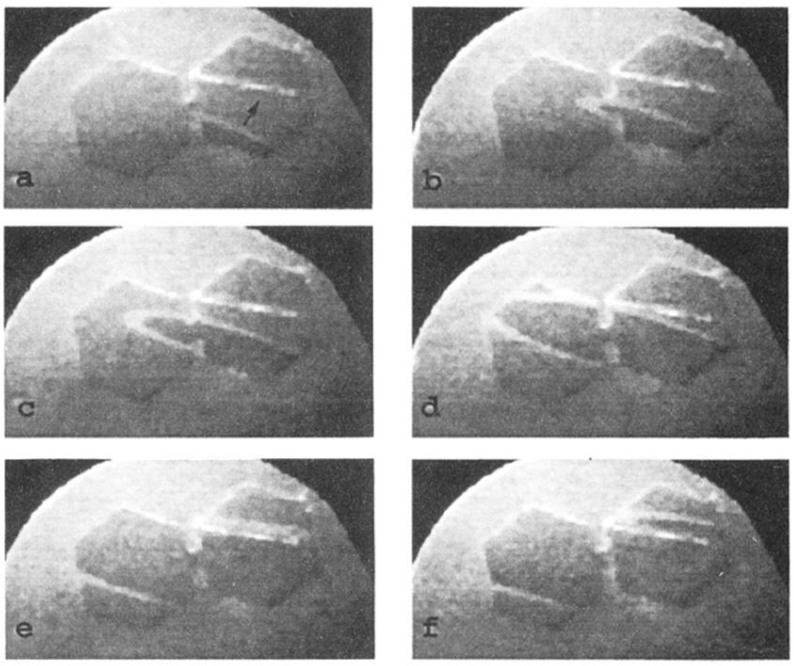

FIG. 17. A pulse starts at the bottom of the right hexagon and moves through the opening into the left hexagon. The parameters are $p_{CO}=1.08\times10^{-4}$ mbar, $p_{O_2}=4.0\times10^{-4}$ mbar, and $T=489$ K. The height of the hexagons is 100 μm and the time interval between frames is 1.5 s.

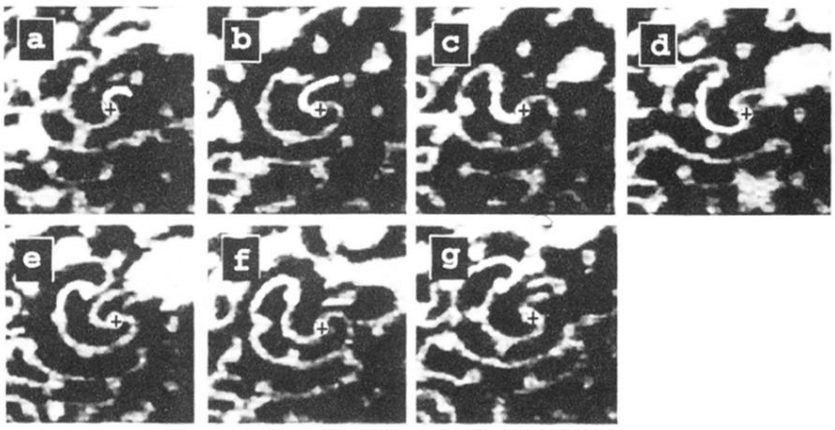

FIG. 18. The pinned spiral rotates counterclockwise around a grid element (marked with a cross) and becomes attached to a second element, where it rotates clockwise. The conditions are $p_{CO}=2.4\times10^{-5}$ mbar, $p_{O_2}=4.0\times10^{-4}$ mbar, and $T=425$ K. The distance between the grid elements is 20 μm.

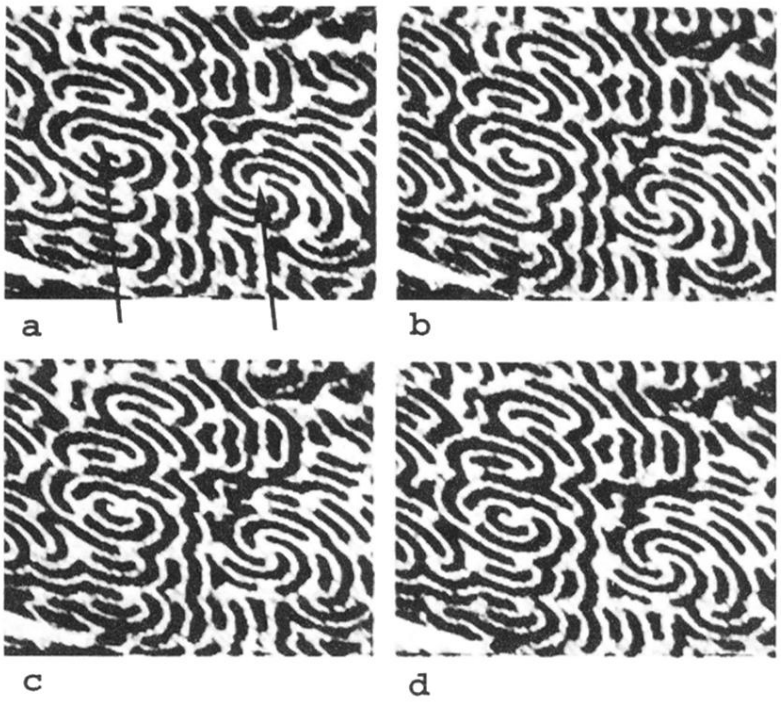

FIG. 19. Wave pattern in the grid created by a free spiral (left arrow) and a multiarmed spiral (right arrow). The conditions are $p_{CO}=2.4\times10^{-5}$ mbar, $p_{O_2}=4.0\times10^{-4}$ mbar, and $T=425$ K. The distance between the grid elements is 20 μm and the time between two frames is 30 s.

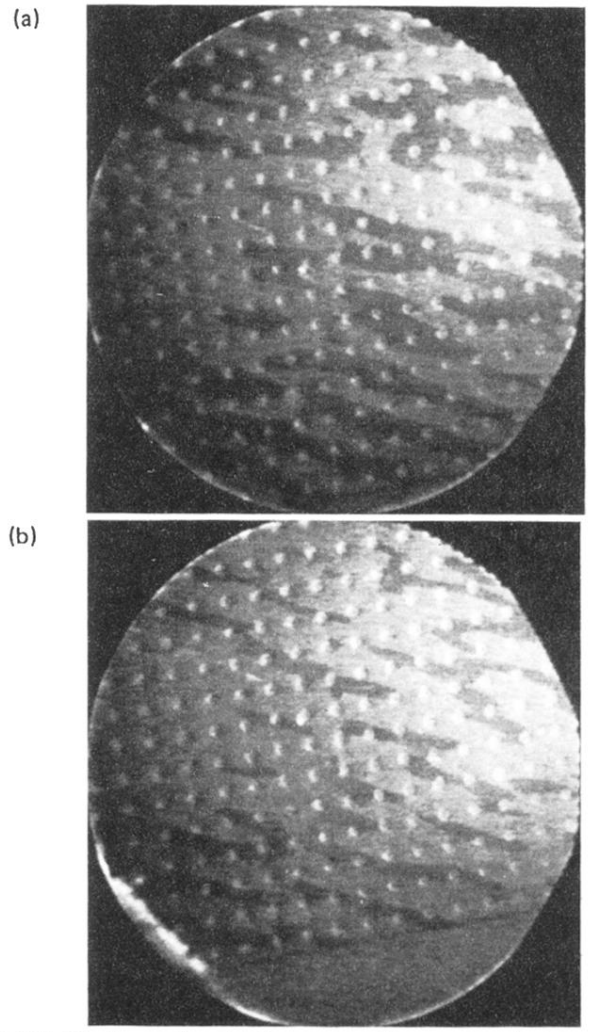

FIG. 20. Examples of solitary-wave-like patterns in the grid. The conditions for both pictures are $p_{CO}=9.7\times10^{-5}$ mbar, $p_{O_2}=4.0\times10^{-4}$ mbar, and $T=485$ K.

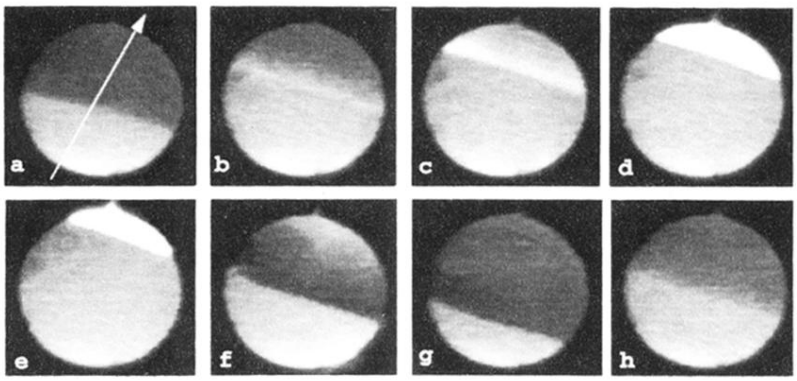

FIG. 21. "Bouncing" of fronts in a circular domain. The bright areas at the top of (d) and (e) indicate the formation of subsurface oxygen. The control parameters are $p_{CO}=2.4\times10^{-5}$ mbar, $p_{O_2}=4.0\times10^{-4}$ mbar, and $T=457$ K. The diameter of the circular domain is 100 μm.

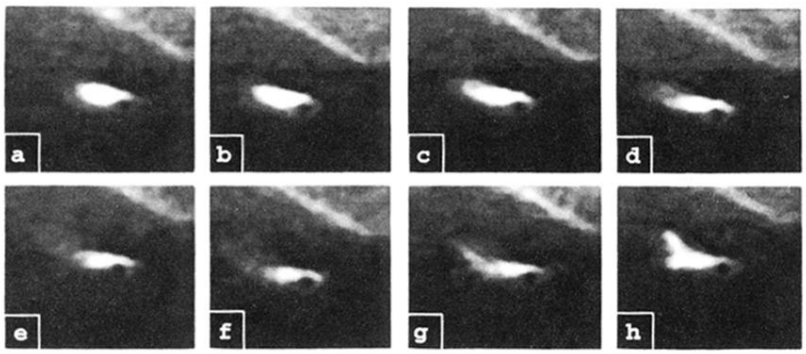

FIG. 23. Flamelike behavior of subsurface oxygen (white) on a CO-covered surface (dark gray). The conditions are $p_{CO}=7.9\times10^{-5}$ mbar, $p_{O_2}=4.0\times10^{-4}$ mbar, and $T=522$ K. The picture size is 50×45 μm^2.

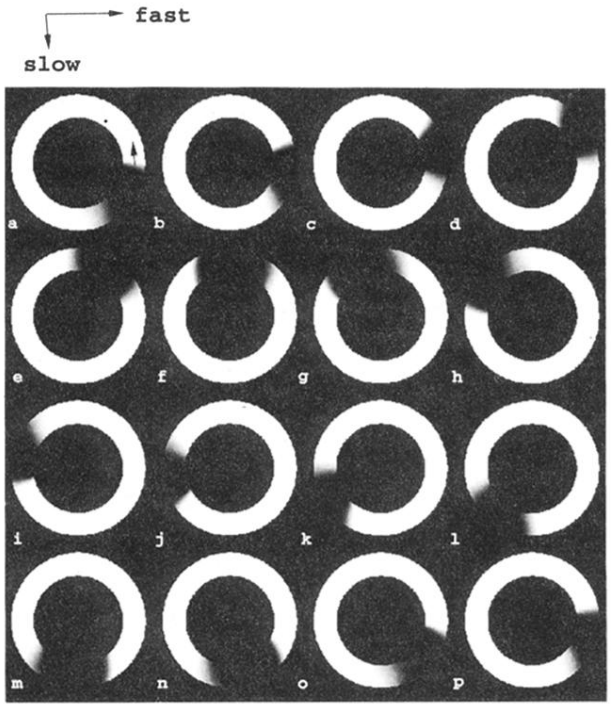

FIG. 24. Simulation of a pulse in a ring with model equations (1)–(3) under excitable conditions ($a=0.84$, $b=0.07$, and $\epsilon=0.025$). The width of the ring is 1.5 space units, the inner (outer) radius is 3.0 (4.5). We used 30 mesh points in the radial direction and 400 mesh points in the angular direction. The time interval between pictures is 0.66. One space unit corresponds to 1.2 μm and a time unit to 2 s for $T=450$ K.

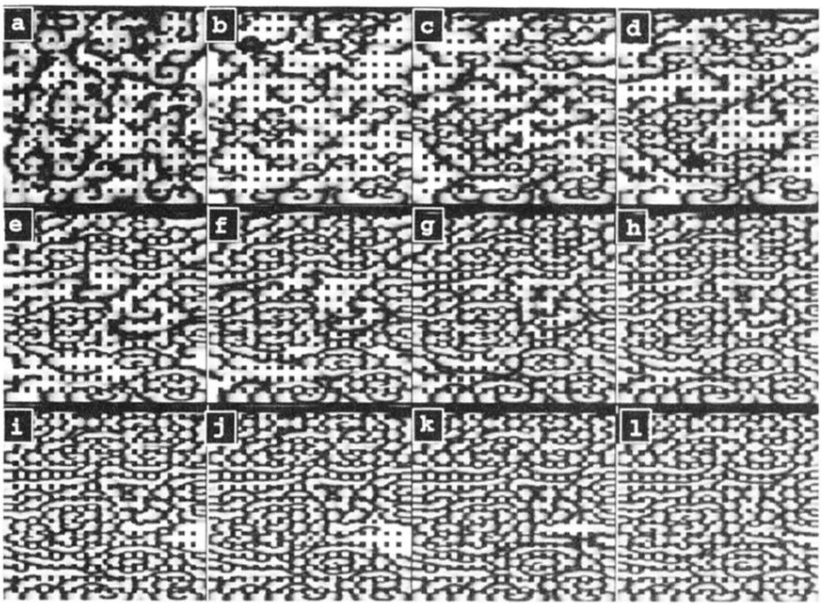

FIG. 26. Simulation of the evolution of waves in a grid with Eqs. (1)–(3), starting from a "turbulent" initial condition containing many spiral wave seeds. The conditions are excitable ($a=0.84$, $b=0.07$, and $\epsilon=0.025$). The time interval between frames is 3.93 and the domain size is 100×100. 256×256 mesh points are used for the integration. The grid elements are squares with a side length of 2.74 and a lattice spacing of 5.94. One space unit corresponds to 1.2 μm and a time unit to 2 s for $T=450$ K.

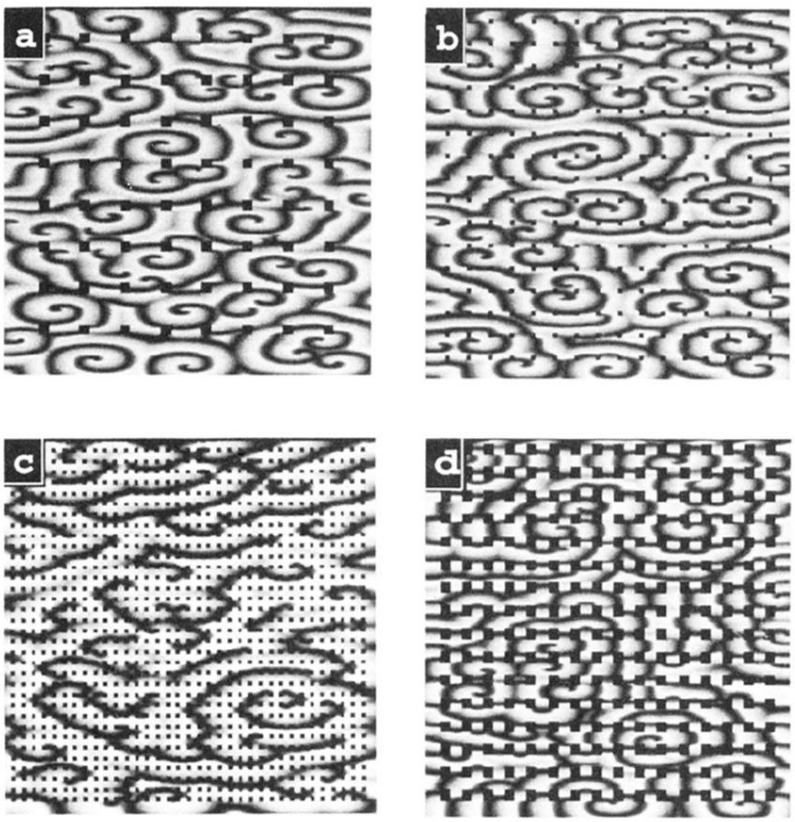

FIG. 27. Wave configurations for varying lattice spacings and element sizes. The parameters and the initial conditions of the integration are identical to Fig. 26. The integration time is 61.5 in (a), (b), and (d) and 615 in (c). (a) The lattice spacing is 10.98 and the square size is 2.74×2.74. (b) The lattice spacing is 5.94 and the square size is 1.18×1.18. (c) The lattice spacing is 2.74 and the square size is 1.18×1.18. (d) The lattice spacing is 5.94 and the square size is 5.94×5.94. One space unit corresponds to 1.2 μm and a time unit to 2 s for $T = 450$ K.

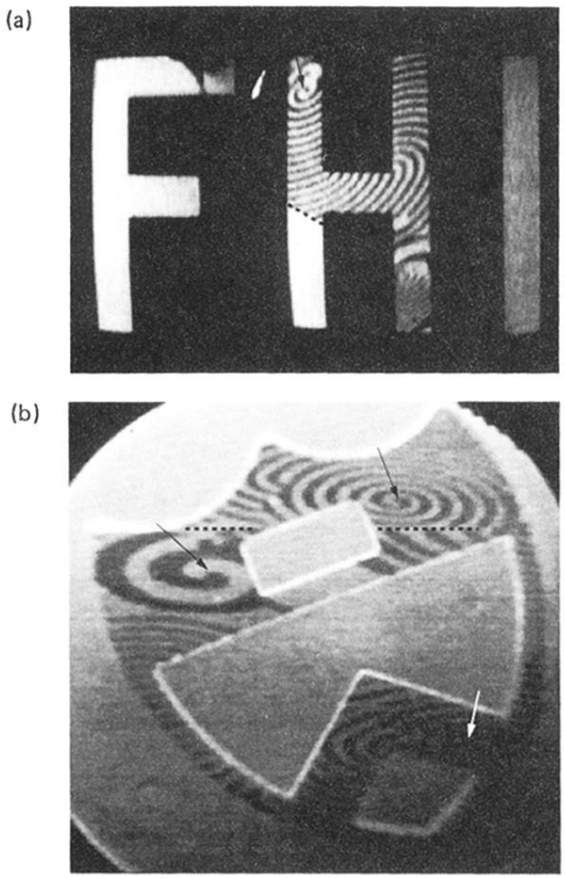

FIG. 3. Examples of large domain patterns: (a) three letter-shaped domains at $p_{CO}=5.0\times10^{-5}$ mbar, $p_{O_2}=4.0\times10^{-4}$ mbar, and $T=440$ K. While the middle one exhibits spiral and periodic wave trains, the left and the right domains are uniformly covered. Spiral cores are marked by arrows, while the location of a scratch is highlighted with a dashed black line. (b) shows a domain in the shape of the Princeton shield with several spiral waves (their tips are marked by arrows) and a large scratch (also marked by a dashed black line). The conditions are $p_{CO}=3.15\times10^{-5}$ mbar, $p_{O_2}=4.0\times10^{-4}$ mbar, and $T=446$ K. Both the letters and the Princeton shield are 350 μm high.

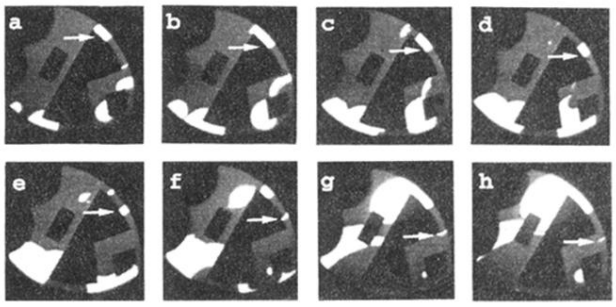

FIG. 4. A sequence in the Princeton shield at conditions in the regime where fronts dominate on the open surface ($p_{CO}=3.05\times10^{-5}$ mbar, $p_{O_2}=4.0\times10^{-4}$ mbar, and $T=446$ K). A pair of fronts, marked by the white arrow, forms a pulse in the small channel at the right-hand side of the shield. Upon exiting this channel, the pulse dies by shrinking. The time interval between the pictures is 15 s for frames $a-g$ and 4 s between frames g and h. The size of the shield is the same as in Fig. 3(b).

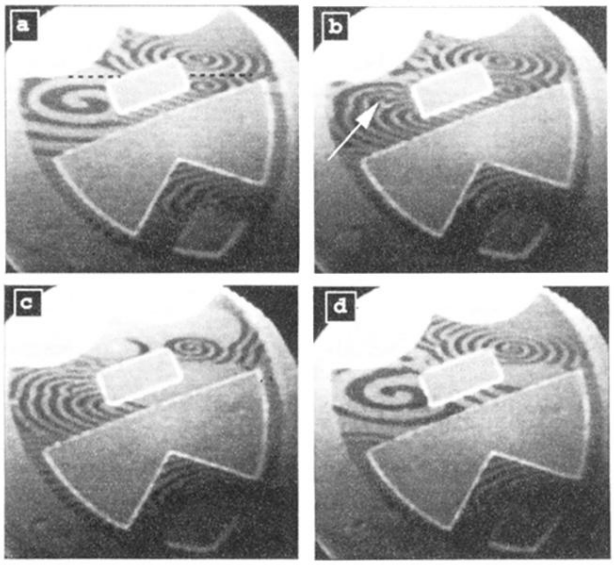

FIG. 5. Subsequent stages of interaction of spirals with each other and with the boundaries in the Princeton shield. The conditions are identical to Fig. 3(b), except that $p_{CO}=3.10\times10^{-5}$ mbar in (a) and (b). A slight change of p_{CO} to 3.15×10^{-5} mbar happens between (b) and (c) and causes the death of the lower spiral of the right-hand-side pair. Again, the scratch is marked with a dashed black line in (a).

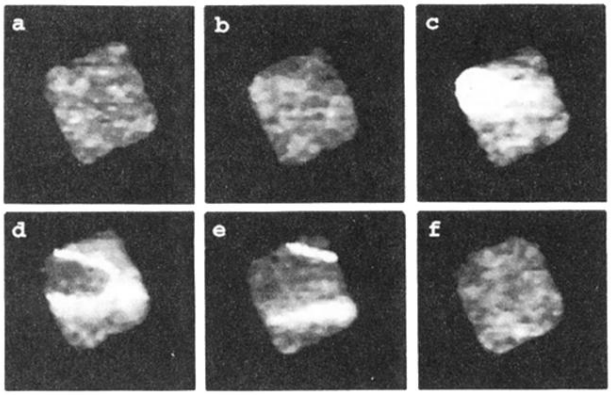

FIG. 6. Pulselike CO waves on a 20×20 μm^2 square. The conditions are $p_{CO}=1.3\times10^{-4}$ mbar, $p_{O_2}=4.0\times10^{-4}$ mbar, and $T=570$ K. The time interval between pictures is 0.2 s.

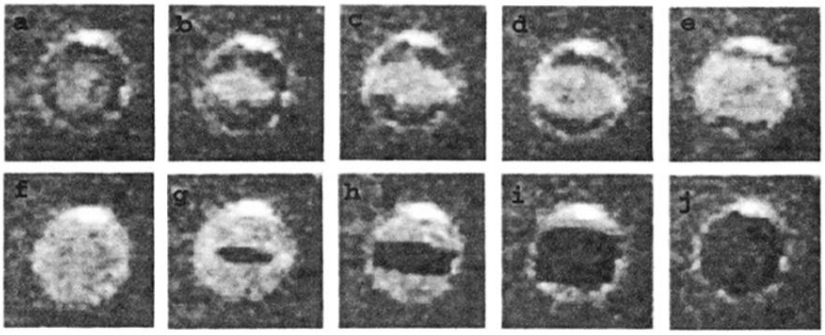

FIG. 8. A two-step event of fronts [a light one in (a) is followed by a dark one in (g)] in a circular geometry with diameter 60 μm. The control parameters are $p_{CO}=9.8\times10^{-5}$ mbar, $p_{O_2}=4.0\times10^{-4}$ mbar, and $T=488$ K. The time interval between frames is 0.25 s.

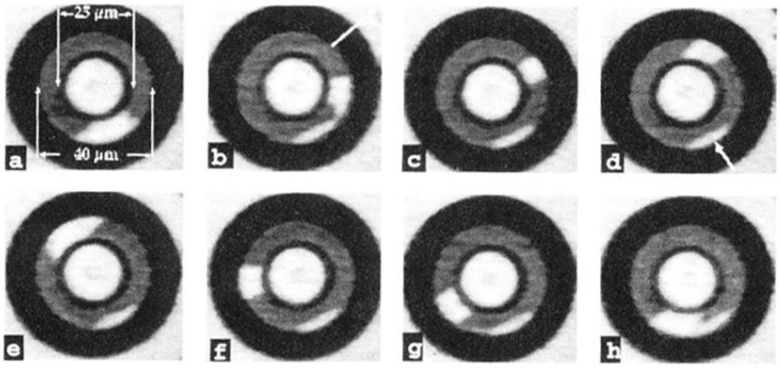

FIG. 9. Isolated CO pulse on a ring at $T=469$ K, $p_{CO}=1.3\times10^{-4}$ mbar, and $p_{O_2}=4.0\times10^{-4}$ mbar. The time interval between frames is 5 s. The white arrow in (b) marks the fast diffusion direction.